Spectrochimica Acta Part A: Molecular and Biomolecular Spectroscopy 226 (2020) 117615

Contents lists available at ScienceDirect

Spectrochimica Acta Part A: Molecular and Biomolecular Spectroscopy

journal homepage: www.elsevier.com/locate/saa

Molecular structure, NLO properties and vibrational analysis of L-Histidine tetra fluro borate by experimental and computational spectroscopic techniques

Nimmy L. John [a,b], Sunila Abraham [a,*], D. Sajan [b], Reji Philip [c], Nithin Joy [c], R.Chitra [d]

[a] Post Graduate & Research Department of Physics, Christian College, Chengannur, Kerala, 689122, India
[b] Centre for Advanced Functional Materials, DST FIST, KSCSTE SARD Supported Post Graduate & Research Department of Physics, Bishop Moore College, Mavelikara, Kerala, 690110, India
[c] Ultrafast and Nonlinear Optics Lab, Light and Matter Physics Group, Raman Research Institute, Sadhashivanagar, Bangalore, 560 080, India
[d] Solid State Physics Division, Bhabha Atomic Research Center, Trombay, Mumbai, 400 085, India

ARTICLE INFO

Article history:
Received 1 April 2019
Accepted 6 October 2019
Available online 8 October 2019

Keywords:
DFT
NBO
AIM
Hirshfeld surface
NLO
Z-scan

ABSTRACT

L-histidine tetra fluroborate (L-HTFB) is a semi-organic NLO material. Ab-initio computations were performed at CAM-B3LYP/ 6–311++g(d,p) level of theory to arrive at the structures, energies, and vibrational wave numbers. The experimental FT-IR and FT-Raman spectra of L-HTFB have been recorded and analyzed. It is compared with the simulated spectra. The scaled wave numbers obtained are in good agreement with the experimental values. Hirshfeld surface analysis represented in the 2D fingerprint plot reveals the interaction within the compound. Optimized geometry reveals that the complexes L -histidine (L-H) and tetrafluoroborate (TFB) are linked by H-F bond which provides inter and intra molecular hydrogen bonded interactions such as N_{10}-$H_{16}\cdots F_{25}$, N_{11}-$H_{17}\cdots F_{22}$, N_{11}-$H_{14}\cdots F_{24}$, N_{11}-$H_{14}\cdots N_{10}$ and N_{11}-$H_{15}\cdots O_{12}$. The inter-molecular distances $H_{17}\cdots F_{22}$, $H_{14}\cdots F_{24}$ and $H_{16}\cdots F_{25}$ are in between 1.82 Å and 2.53 Å. The intra molecular distances $H_{14}\cdots N_{10}$ and $H_{15}\cdots O_{12}$ are found to be at 2.17 Å and 1.71 Å which stabilizes lone pair electron of N_{10} and O_{12} with energies 11.89 and 59.91 KJ/mol respectively. The intra and inter molecular hyperconjugations responsible for the stability of the molecule are well identified theoretically using the NBO analysis. Third order optical nonlinearity is measured by means of the open aperture Z-scan technique which reveals that the crystal has optical limiting property. Photoluminescence results clearly indicate the use of L-HTFB as a new violet-light emitting material.

© 2019 Elsevier B.V. All rights reserved.

1. Introduction

Interest on NLO materials is growing rapidly in connection with the use in various fields such as telecommunication, optical computing, and optical data storage. Unique nature of opto-electronic properties and the use as chemosensors makes the organoboron compounds more attractive in recent researches [1]. $C_6H_{10}O_2N_3$ BF_4 (L-histidine tetra fluroborate, hereafter L-HTFB) crystal is a new synthesized semiorganic NLO material for frequency conversion in the near UV to the near IR.

The structural analysis of LHTFB [2,3] have shown that one N atom in the imidazole ring $(C_3N_2H_4)^+$, and N atom in the amino group (NH_3^+) of the L-histidine $(C_6H_{10}N_3O_2^+)$ complex are protonated at the expense of protons of the tetrafluroboric acid and carboxylic acid. The deprotonation may lead to the existence of carboxylate (COO^-) and tetra fluroborate (BF_4^-) anions. The structural data [3] revealed that BF_4^- anion plays a vital role in N-H···F hydrogen bonding with the histidinium cation via protonated N atoms of imidazole and amino group. The other N atom in the imidazole ring and N atom in the amino group form N-H···O bonds to get stabilization to the compound.

In the present investigation a comparison of theoretical as well as experimental studies of the L-HTFB molecule through the usage of density functional theory, FT-IR, FT-Raman, NMR and UV–Vis spectra have been taken up to understand structure, the nature of vibrations of the different groups, hydrogen bonds and protonation in it. The techniques such as powder-XRD, Z-scan, photoluminescence etc are also employed to get details regarding structure, NLO activity, light emission etc. The analyses such as Hirshfeld Surface, AIM (Atoms In Molecules), Optimized Geometry, NBO (Natural Bond Orbital), NLO, HOMO-LUMO etc are also performed to understand the nature of the interaction in these complexes, stabilization energy, hyperpolarizability, energy gap etc.

2. Experimental procedure

2.1. Preparation

The single crystals of L-HTFB are grown by slow evaporation of aqueous solution of L-histidine $(C_6H_{10}N_3O_2^+)$ and tetrafluoroboric acid

* Corresponding author.
E-mail address: sunila.ayk@gmail.com (S. Abraham).

https://doi.org/10.1016/j.saa.2019.117615
1386-1425/© 2019 Elsevier B.V. All rights reserved.

(BF_4H) in stoichiometric ratio at ambient temperature. The solvent evaporation led to the evolution of free-standing rod like crystals. By water, the material was recrystallized and single crystals were produced. The powder X-ray diffraction (PXRD) was carried out for the structural characterization of L-HTFB crystal.

2.2. Spectroscopic measurements

The powder X-ray diffraction (PXRD) data is obtained using the Rigaku MinFlex 600 table top XRD diffractometer. FT-IR spectrum is recorded in the range 4000-500 cm^{-1} on a Perkin Elmer-paragon-500 FTIR spectrophotometer with 1 cm^{-1} spectral resolution with the sample in KBr. The FT-Raman spectrum is recorded on a Bruker RFS 27 spectrometer with 100 mW laser power and a resolution of 2 cm^{-1} in the range 50–4000 cm^{-1}. Open-aperture Z-scan method is used to study the non-linear absorption behaviour of the sample by using the Q-Switched Nd:YAG laser wavelength of 532 nm, a pulse width of 5 ns and an average energy of 150 μJ, [4]. The position of the sample is changed from the positive to the negative in the z-direction with respect to the focus of the beam, and the transmittance value is noted for each position. The UV–Vis absorption spectrum of the sample is recorded in D_2O solution using a JASCO UV–Vis spectrophotometer in the spectral region of 190–1100 nm. Photoluminescence study using the Horba Scientific Inc. spectrophotometer is carried out at room temperature with an excitation wavelength of 350 nm on a Xe lamp as the excitation source. The powdered sample is mixed in D_2O and mounted inside the chamber for the measurements. The ^1H and ^{13}C NMR spectral analysis are carried out in heavy water (D_2O) by using 400 MHz Bruker AC 200 and 500 MHz Bruker Avance III NMR spectrometer.

3. Computational details

The density functional theory calculation (DFT) along with normal coordinate analysis has been performed to predict the molecular structure as well as the complete vibrational spectra. In the present investigation the DFT study of L-HTFB has been carried out with a new hybrid exchange correlation functional level using the Coulomb-Attenuating Method CAM-B3LYP [5] with the standard basis set 6–311++g(d,p) level [6] through Gaussian 09W software package [7]. It is established to compute natural bond orbital (NBO) interactions and non-linear optical (NLO) activity of the isolated molecule. The normal coordinate analysis has been accurately encoded to generate the complete assignments of various vibrations that are aware of the chemical structural environment of the molecule. It is also appended to the potential energy distribution (PED) of the harmonic vibration spectra which is constructed by the provision of a scaled quantum mechanical (SQM) force field and the procedure is reiterated using MOLVIB program version 7.0 written by Sundius [8] until the RMS frequency error became < 10. The appraisal of intra, inter molecular interactions, donor - acceptor energy relations of L-HTFB were adopted from the NBO analysis using the NBO 5.0 program [9]. The highest occupied molecular orbital (HOMO) and lowest unoccupied molecular orbital (LUMO) energy calculations in L-HTFB give rise to information regarding the energy gap, ionisation potential (IP), electron affinity (EA), overall energy balance (EB), total energy change (TEC), electronegativity (χ), chemical potential (μ), electrophilicity index (Ψ), chemical hardness (η) and global softness (S). The electronic transitions of the L-HTFB is interpreted using the experimental UV–Vis spectrum in D_2O solvent phase compared with the simulated spectra in D_2O solvent phase as well as gas phase. The open-aperture Z-scan analysis was carried out to study the non-linear absorption behaviour of L-HTFB crystal. The NMR analysis provides the structural confirmation of the L-HTFB compound.

4. Results and discussion

4.1. Powder XRD (p-XRD) studies

The crystal of the L-HTFB molecule is shown in Fig. 1. In order to confirm the structure of the crystal, its experimentally obtained powder XRD pattern (Fig. 2-a) and the CIF file generated single crystal XRD pattern (Fig. 2-b) are compared with the powder XRD data reported earlier [10]. The patterns are in good agreement.

4.2. Hirshfeld Surface analysis

This analysis is mainly focused on finding the contribution of atoms in intermolecular interactions. The d_{norm} surface is used to identify the close contact inter and intra molecular interaction in the molecule. The d_{norm} surface of L-HTFB in the Fig. 3-a reveals that the O_{12}, H_{15}, H_{16}, and H_{17} atoms are taken part in inter molecular interaction with the nearest molecule. The percentage contribution of each intermolecular interaction towards the total Hirshfeld surface area (Fig. 3-b) is represented in the 2D fingerprint plot. The major part 43.6% of the contribution is from HF interactions (Fig. 3-c), 24.3% from OH interaction (Fig. 3-d), and 15.8% from HH interactions (Fig. 3-e).

4.3. Optimized geometry

The L-Histidine molecule protonated at N atom in the imidazole ring is termed as L-Histidinum ($C_6H_{10}N_3O_2^+$) cation [2]. The optimized crystal structure shows protonated five membered imidazole ring $(C_3N_2H_4)^+$ and $(NH_3)^+$ ions counterbalanced with negatively charged carboxylate $(COO)^-$ and tetrafluroborate $(BF_4)^-$ ions. The optimized geometry of the L-histidine (L-H) - tetrafluoroborate (TFB) complex has two stationary structures associated with hydrogen bonding as shown in Fig. 4. The structural parameters of the L-HTFB molecule ensure fairly accurate agreement with the experimental data summarized in Table 1 [3].

The two complexes L-histidine (L-H) and tetrafluoroborate (TFB) are in contact with each other through a link of H···F hydrogen bonded inter molecular interactions (N_{10}-H_{16}···F_{25}, N_{11}-H_{17}···F_{22} and N_{11}-H_{14}···F_{24}) and H···N, H···O hydrogen bonded intra molecular interactions (N_{11}-H_{14}···N_{10} and N_{11}-H_{15}···O_{12}). It creates a structural insight of L-histidine tetra fluroborate compound. The inter-molecular H_{16}···F_{25}, H_{14}···F_{24},H_{17}···F_{22} bond distances 1.98 Å, 2.53 Å and 1.82 Å are within the van der Waals radii (2.67 Å) [11]. Therefore, the intermolecular hydrogen bonded interactions along with its corresponding angles 152.57°, 153.98° are raised into a strong bond category as it falls close to the statistical scope level ~160° for biological molecules [12]. In the

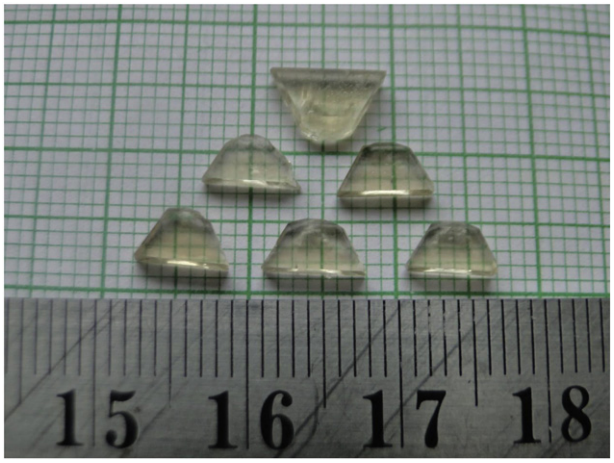


Fig. 1. Photograph of Grown crystal L-HTFB.

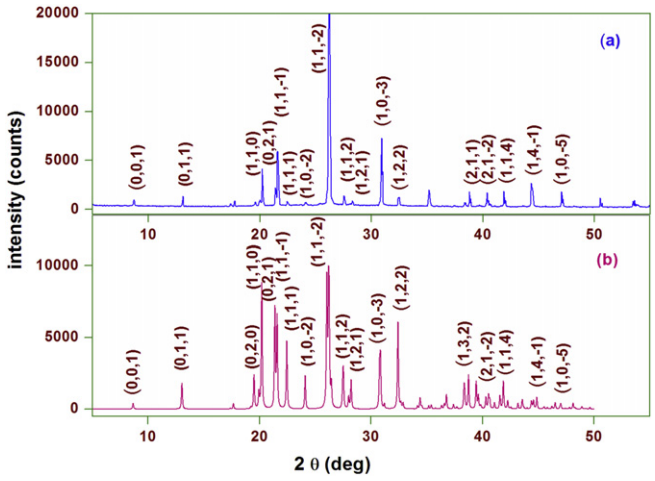


Fig. 2. (a) powder XRD pattern and (b) single crystal XRD pattern of L-HTFB.

intra molecular N_{11}-H_{14}···N_{10} interaction, the H_{14}···N_{10} bond distance 2.17 Å is nearly within the van der Waals radii 2.7 Å [11]. In the intra molecular N_{11}-H_{15}···O_{12} interaction, the H_{15}···O_{12} bond distance 1.71 Å is within its van der Waals radii 2.68 Å [11]. The C_8-O_{12} bond length slightly increases due to the intra molecular interaction between O_{12} of COO^- and H_{15} of NH_3^+ group. The bond C_{10}-N_1 and C_9-N_1 elongates nearly 0.09 Å due to the protonation take place in the imidazole ring. The F_{25}-B_{26} bond shrinks nearly 0.05 Å in $(BF_4)^-$ ion due to the intermolecular interactions in addition to protonation. The inter and intra molecular interactions show that the positive charge of protonated cation of imidazole and amino $(NH_3)^+$ groups are balanced with the negative charges of deprotonated anion of the carboxylate $(COO)^-$ group and the tetrafluoroborate $(BF_4)^-$ ion leading to increase in stability of the complex. The delocalization of electrons in imidazole ring makes resonance effect and turns the single bond of C_2-C_3 also to nearly typical double bond 1.34 Å. The conversion of single bonds in imidazole ring and carboxylate group to double bond reveals the enhancement of the NLO property of the compound.

The connection between the high electronegative nitrogen and fluorine atom through hydrogen bond enhances the strength of the N-H bond [13]. The expansion of B-F bonds (B_{26}-F_{22}, B_{26}-F_{24}, B_{26}-F_{25}) to 1.43 Å in TFB is due to inter-molecular interaction and contraction of B_{26}-F_{23} bond to 1.38 Å is due to the absence of inter-molecular interaction in the complex (Table 1). This reveals the strong hydrogen bonded interactions that take place amid L-H and TFB complex.

4.4. NBO analysis

NBO analysis is used to interpret the solutions of computational Schrodinger's wave equation into a known language of chemical bonding concepts in accordance with the occupied Lewis and unoccupied non-Lewis localized orbitals [14]. The hyperconjugative interaction formed by the orbital overlap between an occupied and unoccupied neighboring orbitals causes stabilization effect in the system. The intensive probable interaction with large second order perturbation energy E(2) from the bonding orbital (donor) to the anti-bonding orbital (acceptor) are included in the Table 2. Generally, the hydrogen bonding interactions with a wide range of stabilization energy in between 2 - 170 KJ/mol have biological importance as in drug designing [15].

The L-histidine structure and tetrafluroborate structure of L-HTFB complex are mentioned as unit 1 and unit 2 respectively in the Table 2. The inter-molecular interactions were taken place from unit 2 to unit 1. Among this, the first and third lone pair electron of fluorine (F_{22}) transfers into the anti-bonding σ orbital of N_{11}-H_{17} with respective interaction energy 3.60 KJ/mol and 25.16 KJ/mol creates N_{11}-H_{17}···F_{22} interaction. Also, the first and third lone pair electrons of F_{24} atom transfer its electrons into each σ anti-bonding orbital of N_{11}-H_{14} with

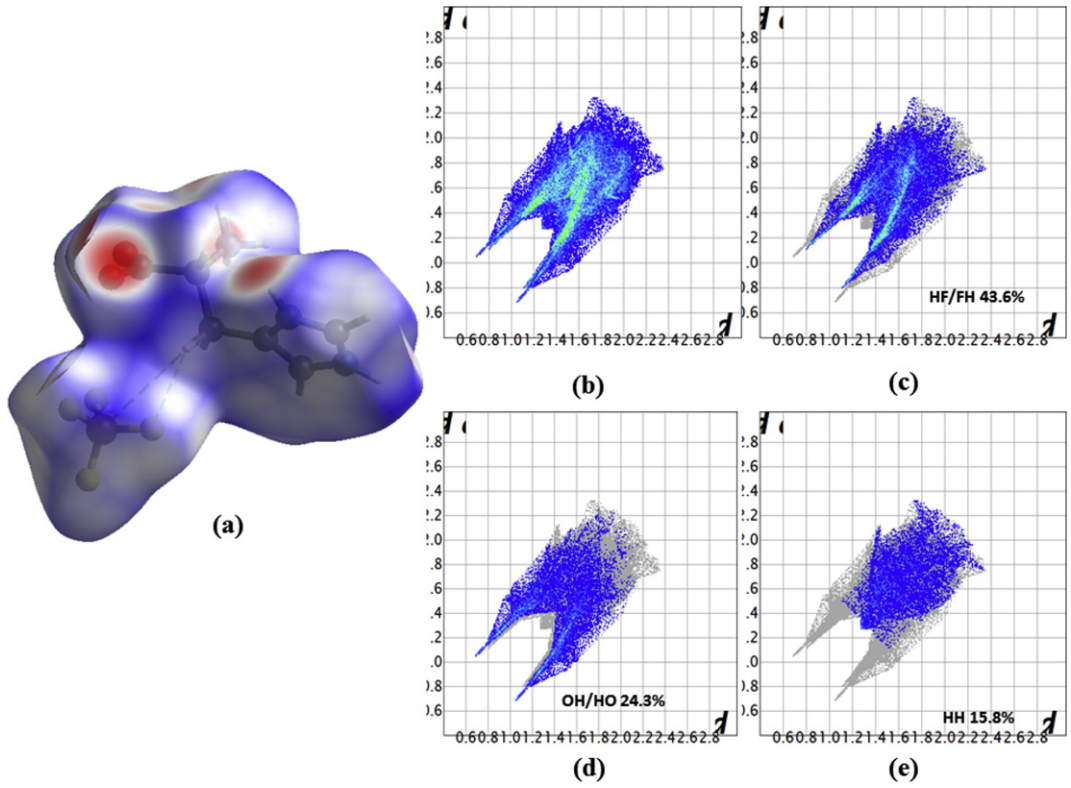


Fig. 3. (a) d_{norm} surface of L-HTFB (b) 2D fingerprint plot towards the total Hirshfeld surface (c) Percentage of HF contribution (d) Percentage of OH contribution (e) Percentage of HH contribution of L-HTFB.

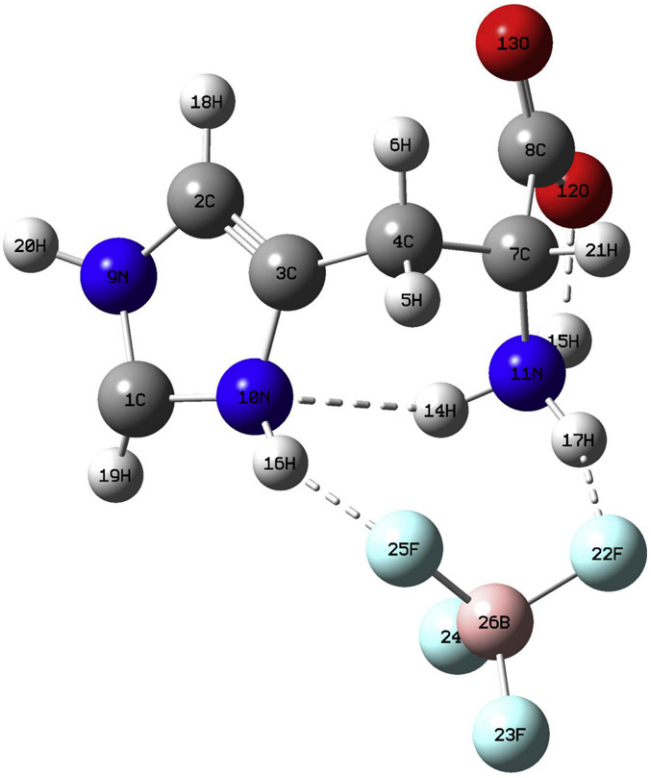


Fig. 4. Optimized geometry structure of L-HTFB.

energy 2.96 KJ/mol forms N_{11}-H_{14}···F_{24} interaction. Finally, the first and third lone pair electrons of fluorine (F_{25}) transfer into the σ*(N_{10}-H_{16}) with respective interaction energy 3.43 KJ/mol and 11.26 KJ/mol causes N_{10}-H_{16}···F_{25} interaction. This means that the contributions of the three highly electronegative fluorine atoms provide more support for the stable conformation of the title molecule. These three strong intermolecular interactions create a bridge between the two units in complex L-HTFB.

The strong intra-molecular interactions in the unit 1 that mainly occur in the imidazole ring and carboxylate group produce resonance effect. The strong stabilizing delocalization and resonance structure in the imidazole ring occurs as double bond in C_2=C_3 through the transfer of localized lone pair electron of N_9 and N_{10} to delocalize adjacent π* antibond orbital of C_2-C_3 with respective stabilization energy 35.13 KJ/mol and 47.69 KJ/mol. Thus the electron from π orbital of C_2-C_3 donate to the σ*orbital of N_{10}-H_{16} with stabilization energy 5.44 KJ/mol. This shows protonization in the imidazole ring. The carboxylate group undergoes charge delocalization by means of second lone pair electron transfer from O_{13} to σ*orbital of C_8-O_{12} and also from O_{12} to σ*orbital of C_8-O_{13} with respective interaction energy 52.29 and 45.18 KJ/mol are evident in optimized structure as double bond instead of single bond. Also, the intramolecular interaction energy within the carboxylate group involves electron transfer from third lone pair of oxygen O_{13} to the π antibonding C_8-O_{12} orbital with maxima energy 351.73 KJ/mol. Thus it takes part in the π→ σ* interaction from the π orbital of C_8-O_{12} bond to the σ*orbital of C_8-O_{13} bond in the carboxylate group with energy 5.36 KJ/mol. The first and second lone pair of the O_{12} transfer electron to the σ anti-bonding orbital of N_{11}-H_{15} with stabilization energy 8.12 and 51.79 KJ/mol respectively which causes N_{11}-H_{15}···O_{12} intra molecular interaction. The lone pair electron of N_{10} transfer into σ*(N_{11}-H_{14}) with respective interaction energy 11.89 KJ/mol which causes N_{11}-H_{14} ··· N_{10} interaction.

According to TFB in unit 2, the electron density in the order F_{22}-B_{26} > F_{25}-B_{26} > F_{24}-B_{26} > F_{23}-B_{26} by the value 0.042 e > 0.040 e > 0.037 e > 0.033 e through the F_{22}, F_{23}, F_{24}, F_{25} lone pair interaction which reveals that as per the criteria of strong inter molecular interaction with short F···H distance, the corresponding electron density of F-B bond (~1.43 Å) increases. The bond F_{23}-B_{26} (1.38 Å) without inter molecular interaction has less electron density when compared to other F-B bond with inter molecular interaction. This reveals the hydrogen bonded interactions are strong in the order N_{11}-H_{17}···F_{22} > N_{10}-H_{16}···F_{25} > N_{11}-H_{14}···F_{24}.

These discloses the counterbalance of the protonated cation and the negative charges of deprotonated anion. The important hyperconjugative interactions that occur between σ donor and σ* acceptor are also mentioned in the Table 2. NBO analysis gives evidence for the existence of C_2=C_3 double bond as well as protonated N atom in the imidazole ring which leads to the characteristic NLO property.

4.5. NMR analysis

The proton and carbon nuclei involved in the formation of L-HTFB were recorded in the Fig. 5, Fig. 6. The ^{1}H and ^{13}C NMR spectral analysis of L-HTFB compound was carried out in heavy water (D_2O) by using 400 MHz Bruker AC 200 and 500 MHz Bruker Avance III NMR spectrometer. The ^{13}C and ^{1}H chemical shifts were done in gas as well as in D_2O phase by using the basis set CAM-B3LYP/6–311++g(d,p). The experimental spectrum of the simulated and observed ^{13}C and ^{1}H chemical shifts are reported in the Table 3. The carbon atom C_4 and C_7 in the ethyl group, have small singlet chemical shift at 53.56 and 25.74 ppm as observed. The large ^{13}C chemical shift occur in the carbon atom of ethyl-substituted COO^- group at 176.53 ppm in D_2O and 179.25 ppm in gas phase is in correlation with its singlet experimental shift 172.52 ppm. Also, the carbon atom C_3, C_1, C_2 in the ethyl-substituted imidazole ring structure has corresponding experimental chemical shifts at 134.03, 127.40, 117.73 ppm. The highest ^{1}H chemical shift in the L-HTFB molecule is observed as doublet at 8.62 δ in H_{17} hydrogen interlinked H···F interaction and in H_{15} hydrogen interlinked O···H interaction. The next highest chemical shift is observed as singlet at 7.36 δ in H_{16} hydrogen atom of the imidazole ring in which the H···F interaction takes place. For the other two imidazole hydrogen H_{18}, H_{19}, H_{20} the chemical shifts are observed at 4.02, 4.01, and 3.33 δ respectively which shows the protonation of the N atom. The hydrogen H_{14} of one of the NH_3^+ group which is in connection with fluorine F_{24} arises chemical shift at 3.99 δ. The ethyl group hydrogen atoms H_{21}, H_6, H_5 are observed at ~3.32 δ. The observed and calculated spectra are in good agreement with each other. NMR spectral analysis of the compound also gives evidence for deprotonation of COO^- and protonation of NH_3^+ group and N atom of imidazole ring.

4.6. Hyperpolarizability and vibrational contribution to NLO activity

The non-linear optical field is developing vastly in modern times due to the enhancement of hyperpolarizability that has been discovered in various molecules. Hence, the investigation of enhancement of hyperpolarizability and structure of the title compound through the vibrational analysis is important. The conjugated π electrons within the molecule are categorized using large value of first order molecular hyperpolarizability [16,17]. Its tensor components are calculated using Gaussian software in DFT approach and summarized in Table S1. It is found that there are six components for the linear polarizibility, ten for static first hyperpolarizability, eighteen for the dynamic first hyperpolarizability, fifteen for static second hyperpolarizability, thirty six for quadratic electro optic Kerr effect and fifty four for the electric-field-induced second-harmonic generation.

The calculations of the total dipole moment as well as static and dynamic values of linear polarizability, anisotropy, first order hyperpolarizability and second order hyperpolarizability using the basis set B3LYP/ cc-pVTZ (Table 4) are also made. All these calculated values are high when compared to that of urea, a prototypical NLO

Table 1
Optimized bond lengths, bond angles and dihedral angles of LHTFB by CAM-b3lyp/6–311++g(d,p) in comparison with the XRD data.

Bond length	Expt(Å)	Calc(Å)	Bond angle	Expt(/°)	Calc(/°)	Dihedral angle	Expt(/°)	Calc(/°)
C1-N9	1.33	1.42	N9-C1-N10	107.68	104.07	N10-C1-N9-C2	1.10	-16.56
C1-N10	1.32	1.41	N9-C1-H19	127.53	118.01	N10-C1-N9-H20	179.38	-154.48
C1-H19	1.08	1.09	N10-C1-H19	124.68	117.81	H19-C1-N9-C2	-175.25	-149.26
C2-C3	1.37	1.34	C3-C2-N9	106.87	109.00	H19-C1-N9-H20	3.04	72.82
C2-N9	1.38	1.40	C3-C2-H18	130.87	128.43	N9-C1-N10-C3	-1.25	16.71
C2-H18	1.07	1.08	N9-C2-H18	122.25	122.20	N9-C1-N10-H16	-172.71	160.46
C3-C4	1.49	1.49	C2-C3-C4	130.51	130.93	H19-C1-N10-C3	175.23	149.52
C3-N10	1.38	1.40	C2-C3-N10	105.94	108.12	H19-C1-N10-H16	3.77	-66.73
C4-H5	1.09	1.09	C4-C3-N10	123.55	120.58	N9-C2-C3-C4	-179.92	172.86
C4-H6	1.09	1.09	C3-C4-H5	110.44	109.19	N9-C2-C3-N10	-0.22	0.04
C4-C7	1.54	1.53	C3-C4-H6	108.10	109.61	H18-C2-C3-C4	-0.07	-0.08
C7-C8	1.55	1.57	C3-C4-C7	114.66	113.60	H18-C2-C3-N10	179.64	-172.90
C7-N11	1.46	1.49	H5-C4-H6	106.00	108.70	C3-C2-N9-C1	-0.53	10.62
C7-H21	1.09	1.09	H5-C4-C7	107.60	109.79	C3-C2-N9-H20	-178.79	148.18
C8-O12	1.33	1.26	H6-C4-C7	109.70	105.81	H18-C2-N9-C1	179.60	-175.91
C8-O13	1.25	1.23	C4-C7-C8	108.45	114.47	H18-C2-N9-H20	1.34	-38.35
N9-H20	1.01	1.01	C4-C7-N11	116.93	113.56	C2-C3-C4-H5	101.05	142.21
N10-H16	1.05	1.02	C4-C7-H21	108.94	109.10	C2-C3-C4-H6	-14.50	23.23
N11-H14	1.01	1.03	C8-C7-N11	110.27	105.50	C2-C3-C4-C7	-137.20	-94.88
N11-H17	1.02	1.03	C8-C7-H21	104.74	106.85	N10-C3-C4-H5	-78.61	-45.72
H16-F25	1.56	1.98	N11-C7-H21	106.83	106.91	N10-C3-C4-H6	165.84	-164.69
H17-F22	1.99	1.82	C7-C8-O12	113.29	113.02	N10-C3-C4-C7	43.14	77.19
F22-B26	1.41	1.43	C7-C8-O13	123.08	116.16	C2-C3-N10-C1	0.91	-10.78
F23-B26	1.36	1.38	O12-C8-O13	123.62	130.78	C2-C3-N10-H16	171.88	-155.05
F24-B26	1.41	1.41	C1-N9-C2	109.23	107.54	C4-C3-N10-C1	-179.36	175.51
F25-B26	1.47	1.42	C1-N9-H20	124.70	118.10	C4-C3-N10-H16	-8.39	31.25
O12..H15	2.69	1.71	C2-N9-H20	126.05	118.84	C3-C4-C7-C8	-177.49	73.06
N11-H15	0.90	1.06	C1-N10-C3	110.27	108.30	C3-C4-C7-N11	57.13	-48.19
			C1-N10-H16	122.27	120.91	C3-C4-C7-H21	-64.03	-167.31
			C3-N10-H16	126.83	119.72	H5-C4-C7-C8	-54.21	-164.36
			C7-N11-H14	113.08	111.77	H5-C4-C7-N11	-179.58	74.39
			C7-N11-H17	112.72	113.53	H5-C4-C7-H21	59.25	-44.73
			H14-N11-H17	109.46	107.00	H6-C4-C7-C8	60.68	-47.23
			N10-H16-F25	166.87	152.57	H6-C4-C7-N11	-64.70	-168.47
			N11-H17-F22	168.74	153.98	H6-C4-C7-H21	174.13	72.41
			H17-F22-B26	127.26	101.75	C4-C7-C8-O12	-145.50	-138.63
			H16-F25-B26	102.45	117.03	C4-C7-C8-O13	35.72	43.29
			F22-B26-F23	112.90	110.56	N11-C7-C8-O12	-16.30	-13.05
			F22-B26-F24	109.03	107.22	N11-C7-C8-O13	164.92	168.87
			F22-B26-F25	105.69	107.64	H21-C7-C8-O12	98.30	100.48
			F23-B26-F24	113.15	112.06	H21-C7-C8-O13	-80.49	-77.60
			F23-B26-F25	109.83	111.12	C4-C7-N11-H14	30.24	25.15
			F24-B26-F25	105.75	108.04	C4-C7-N11-H17	-94.59	-96.00
			C8-O12-H15	104.87	79.51	C8-C7-N11-H14	-94.23	-101.00
			C7-N11-H15	112.58	99.71	C8-C7-N11-H17	140.95	137.86
			H14-N11-H15	104.22	109.40	H21-C7-N11-H14	152.50	145.51
			H15-N11-H17	120.27	115.39	H21-C7-N11-H17	27.68	-98.94
						C1-N10-H16-F25	63.86	170.16
						C3-N10-H16-F25	-106.11	-50.11
						C7-N11-H17-F22	18.13	70.80
						H14-N11-H17-F22	-108.64	-52.98
						N10-H16-F25-B26	-17.70	-71.02
						N11-H17-F22-B26	-32.65	49.15
						H17-F22-B26-F23	-114.43	161.93
						H17-F22-B26-F24	118.91	39.50
						H17-F22-B26-F25	5.64	-76.52
						H16-F25-B26-F22	64.62	103.19
						H16-F25-B26-F23	-173.32	-135.62
						H16-F25-B26-F24	-50.92	-12.30
						C7-C8-O12-H15	4.01	5.69
						O13-C8-O12-H15	-177.21	-176.58
						C4-C7-N11-H15	52.41	140.70
						C8-C7-N11-H15	-69.16	14.55
						H21-C7-N11-H17	-52.30	24.37
						H15-N11-H17-F22	121.59	-174.97

active molecule. The theoretical dipole moment value for isolated gas phase of L-HTFB molecule was 10.9844 Debye which is 2.94 times that of urea [18], a prototypical NLO active molecule. The static and dynamic isotropic polarizabilities (<α>) are 3.57 and 3.65 times that of urea. Also, the frequency dependent static and dynamic anisotropic polarizability values predicted (Δα) are 3.25 and 3.42 times than that of urea. The static -first and second order hyperpolarizability ($\beta(0;0,0)$ and $\gamma(0;0,0,0)$) are 5.41 and 4.79 times that of urea. The frequency dependent first hyperpolarizability values for the electro-optical Pockels effect and second hyperpolarizability values for the quadratic electro optic Kerr effect ($\beta(-\omega;\omega,0)$and $\gamma(-\omega;\omega,0,0)$) are 6.67 and 6.18 times than that of urea. The orientationally arranged theoretically

Table 2
Second order perturbation theory analysis of Fock matrix in NBO basis of LHTFB.

Donor(i)	ED(i) (e)	Acceptor(j)	ED(j) (e)	E(2)[a] (KJ/mol)	E(j)-E(i)[b] (a.u)	F(i,j)[c] (a.u)
unit 1						
σ(C1-N9)	0.994	σ*(C2-H18)	0.006	6.11	1.32	0.056
σ(C1-N9)	0.994	σ*(N10-H16)	0.014	4.98	1.32	0.05
σ(C1-N10)	0.993	σ*(C3-C4)	0.011	8.37	1.33	0.065
σ(C1-N10)	0.993	σ*(N9-H20)	0.010	4.61	1.3	0.048
σ(C1-H19)	0.994	σ*(C2-N9)	0.007	4.81	1.08	0.045
σ(C1-H19)	0.994	σ*(C3-N10)	0.014	5.19	1.09	0.047
σ(C2-C3)	0.991	σ*(C2-H18)	0.006	4.86	1.27	0.049
σ(C2-C3)	0.991	σ*(C3-C4)	0.011	8.42	1.27	0.064
π(C2-C3)	0.980	σ*(C4-H5)	0.008	4.73	0.85	0.039
π(C2-C3)	0.980	σ*(C4-C7)	0.012	6.03	0.83	0.044
π(C2-C3)	0.980	σ*(N9-H20)	0.010	7.24	0.85	0.049
π(C2-C3)	0.980	σ*(N10-H16)	0.014	5.44	0.88	0.043
σ(C2-N9)	0.993	σ*(C3-C4)	0.011	11.43	1.35	0.077
σ(C2-H18)	0.991	σ*(C1-N9)	0.006	6.15	1.07	0.05
σ(C2-H18)	0.991	σ*(C2-C3)	0.020	5.82	1.27	0.053
σ(C2-H18)	0.991	σ*(C3-N10)	0.014	7.12	1.11	0.055
σ(C3-C4)	0.988	σ*(C1-N10)	0.006	5.32	1.2	0.049
σ(C3-C4)	0.988	σ*(C2-C3)	0.020	8.67	1.38	0.068
σ(C3-N10)	0.991	σ*(C2-H18)	0.006	7.45	1.34	0.062
σ(C4-H5)	0.988	σ*(C2-C3)	0.020	5.11	1.22	0.049
σ(C4-H5)	0.988	π*(C2-C3)	0.092	10.34	0.72	0.055
σ(C4-H5)	0.988	σ*(C7-C8)	0.057	6.07	0.98	0.049
σ(C4-H6)	0.984	σ*(C3-N10)	0.014	14.03	1.06	0.075
σ(C4-H6)	0.984	σ*(C7-N11)	0.013	12.31	0.9	0.065
σ(C4-C7)	0.986	σ*(C2-C3)	0.020	4.86	1.35	0.05
σ(C7-H21)	0.985	σ*(C3-C4)	0.011	6.82	1.09	0.053
σ(C7-H21)	0.985	π*(C8-O12)	0.210	8.79	0.66	0.053
σ(C7-H21)	0.985	σ*(N11-H14)	0.015	5.07	1.01	0.044
π(C8-O12)	0.992	σ*(C8-O13)	0.036	5.36	1.07	0.047
σ(C8-O13)	0.994	σ*(C8-O12)	0.031	5.15	1.67	0.058
σ(N11-H15)	0.994	σ*(C4-C7)	0.012	4.77	1.17	0.046
LP(1)C1	0.979	σ*(N9-H20)	0.010	5.44	0.78	0.04
LP(1)N9	0.946	σ*(C1-H19)	0.012	9.84	0.85	0.058
LP(1)N9	0.946	σ*(C2-C3)	0.020	5.69	1.03	0.048
LP(1)N9	0.946	π*(C2-C3)	0.092	35.13	0.52	0.085
LP(1)N10	0.926	σ*(C1-H19)	0.012	9.55	0.83	0.057
LP(1)N10	0.926	σ*(C2-C3)	0.020	5.86	1.01	0.049
LP(1)N10	0.926	π*(C2-C3)	0.092	47.69	0.51	0.097
LP(1)N10	0.926	σ*(N11-H14)	0.015	11.89	0.78	0.061
LP(1)O12	0.987	σ*(C7-C8)	0.057	7.49	1.12	0.058
LP(1)O12	0.987	σ*(N11-H15)	0.036	8.12	1.09	0.059
LP(2)O12	0.924	σ*(C7-C8)	0.057	35.88	0.72	0.1
LP(2)O12	0.924	σ*(C8-O13)	0.036	45.18	0.98	0.133
LP(2)O12	0.924	σ*(N11-H15)	0.036	51.79	0.69	0.119
LP(1)O13	0.989	σ*(C8-O12)	0.031	6.87	1.36	0.06
LP(2)O13	0.938	σ*(C7-C8)	0.057	50.45	0.68	0.115
LP(2)O13	0.938	σ*(C8-O12)	0.031	52.29	0.91	0.137
LP(3)O13	0.774	σ*(C8-O12)	0.031	6.07	0.9	0.051
LP(3)O13	0.774	π*(C8-O12)	0.210	351.73	0.34	0.216
LP(3)O13	0.774	σ*(C8-O13)	0.036	52.42	0.94	0.152
π*(C2-C3)	0.092	σ*(C2-C3)	0.020	20.05	0.5	0.185
π*(C2-C3)	0.092	σ*(C4-H5)	0.008	1.42	0.32	0.041
π*(C2-C3)	0.092	σ*(C4-C7)	0.012	2.55	0.29	0.052
π*(C2-C3)	0.092	σ*(N9-H20)	0.010	1.21	0.32	0.038
σ*(C7-C8)	0.057	σ*(C4-H5)	0.008	3.89	0.06	0.036
σ*(C7-C8)	0.057	σ*(C4-H6)	0.005	1.97	0.07	0.029
σ*(C7-C8)	0.057	σ*(C7-H21)	0.008	1.67	0.06	0.024
σ*(C7-C8)	0.057	σ*(N11-H14)	0.015	1.26	0.01	0.009
σ*(C7-C8)	0.057	σ*(N11-H17)	0.016	3.27	0.03	0.021
π*(C8–O12)	0.210	σ*(C4-C7)	0.012	2.47	0.36	0.039
π*(C8-O12)	0.210	σ*(C7-H21)	0.008	4.40	0.39	0.055
π*(C8-O12)	0.210	σ*(C8-O12)	0.031	4.65	0.56	0.064
unit 2 to unit1						
LP(1)F22	0.995	σ*(N11-H17)	0.016	3.60	1.44	0.045
LP(3)F22	0.972	σ*(N11-H17)	0.016	25.16	0.91	0.094
LP(1)F24	0.996	σ*(N11-H14)	0.015	1.21	1.45	0.011
LP(3)F24	0.978	σ*(N11-H14)	0.015	1.75	0.86	0.016
LP(1)F25	0.995	σ*(N10-H16)	0.014	3.43	1.51	0.045
LP(3)F25	0.977	σ*(N10-H16)	0.014	11.26	0.95	0.064
unit 2						
LP(2)F22	0.982	σ*(F24-B26)	0.037	10.13	0.94	0.061
LP(2)F22	0.982	σ*(F25-B26)	0.040	25.20	0.92	0.095
LP(3)F22	0.972	σ*(F23-B26)	0.033	20.18	1	0.088
LP(3)F22	0.972	σ*(F24-B26)	0.037	13.15	0.97	0.07
LP(2)F23	0.975	σ*(F24-B26)	0.037	23.86	0.92	0.092
LP(2)F23	0.975	σ*(F25-B26)	0.040	26.84	0.91	0.097
LP(3)F23	0.975	σ*(F22-B26)	0.042	34.50	0.89	0.109
LP(3)F23	0.975	σ*(F24-B26)	0.037	9.59	0.92	0.058
LP(3)F23	0.975	σ*(F25-B26)	0.040	7.03	0.91	0.05
LP(2)F24	0.979	σ*(F22-B26)	0.042	18.84	0.9	0.081
LP(2)F24	0.979	σ*(F25-B26)	0.040	24.16	0.91	0.093
LP(3)F24	0.979	σ*(F22-B26)	0.042	10.97	0.9	0.062
LP(3)F24	0.979	σ*(F23-B26)	0.033	27.63	0.96	0.101
LP(3)F24	0.979	σ*(F25-B26)	0.040	5.23	0.92	0.043
LP(2)F25	0.980	σ*(F22-B26)	0.042	25.37	0.91	0.095
LP(2)F25	0.980	σ*(F23-B26)	0.033	15.11	0.96	0.075
LP(3)F25	0.977	σ*(F23-B26)	0.033	10.89	0.98	0.064
LP(3)F25	0.977	σ*(F24-B26)	0.037	24.70	0.95	0.095

predicted frequency dependent first hyperpolarizability values for the second harmonic generation and second hyperpolarizability values for DC electric-field-induced second harmonic generation ($\beta(-2\omega;\omega,\omega)$ and $\gamma(-2\omega;\omega,\omega,0)$) are 25.69 and 83.97 times that of urea. The large value of γ hyperpolarizability, is a measure of the non-linear optical activity associated with the intramolecular charge transfer, resulting from the electron cloud movement through donor-acceptor π

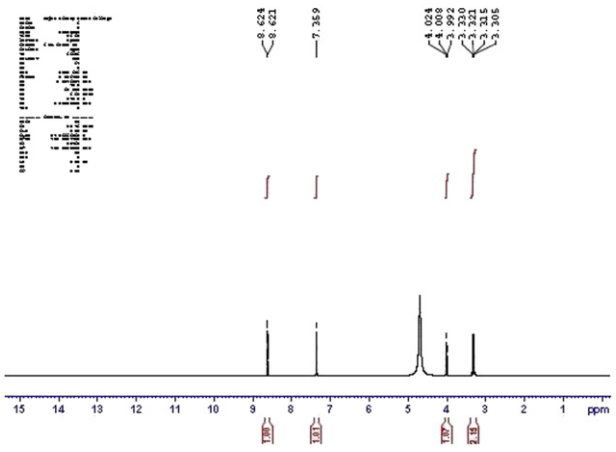


Fig. 5. [1]H NMR spectrum of L-HTFB.

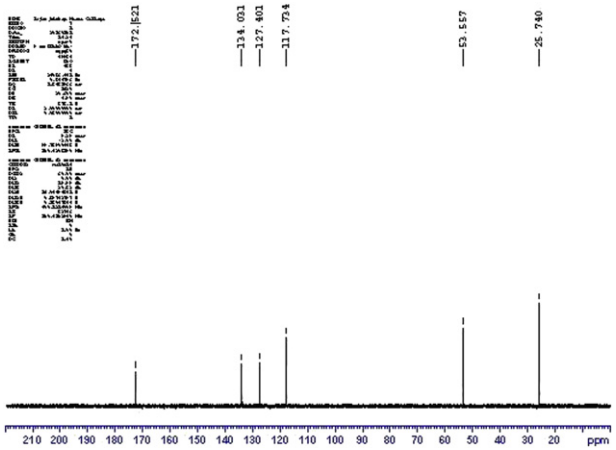


Fig. 6. [13]C NMR spectrum of L-HTFB.

Table 3
Experimental and calculated ^{13}C and ^{1}H NMR chemical shifts (ppm) of LHTFB.

Atom position	CAM-B3LYP (solvent: D2O) Intercept=184.6837 Slope=−0.9685		CAM-B3LYP (solvent: Gas) Intercept=185.2499 Slope=−0.9819		Experimental (D2O)
	Absolute shielding	Chemical shift	Absolute shielding	Chemical shift	Chemical shift
^{13}C					
8	13.70	176.53	9.24	179.25	172.52
3	51.21	137.81	53.03	134.66	134.03
2	67.39	121.11	65.48	121.97	127.40
1	75.95	112.27	76.55	110.70	117.73
7	127.80	58.73	126.88	59.44	53.56
4	160.92	24.53	160.75	24.96	25.74
^{1}H					
	Intercept=31.1423 Slope=−0.9359		Intercept=30.5258 Slope=−0.8349		
15	21.13	10.70	21.39	10.94	8.62
17	24.86	6.72	24.93	6.70	8.62
16	25.07	6.49	25.39	6.15	7.36
18	26.01	5.48	25.86	5.58	4.02
19	26.03	5.46	25.97	5.46	4.01
14	26.63	4.82	26.46	4.87	3.99
20	28.37	2.97	27.40	3.74	3.33
21	28.54	2.78	28.46	2.47	3.32
6	28.87	2.43	28.59	2.32	3.32
5	29.22	2.06	29.15	1.65	3.31

Table 4
Calculated values of nonlinear optical response properties of L-HTFB.

Parameters	Values
Static linear $<\alpha_{(0,0)}>(10^{-24})$ e.s.u	16.3454
Dynamic linear $<\alpha_{(\omega,\omega)}>(10^{-24})$ e.s.u	16.8559
Static Anisotropy $\Delta\alpha$	7.58350
Dynamic Anisotropy $\Delta\alpha$	8.07920
Static First order $<\beta_{(0;0,0)}>(10^{-30})$ e.s.u	3.57316
Dynamic First order $<\beta_{(-\omega;\omega,0)}>(10^{-30})$ e.s.u	4.64100
Dynamic First order $<\beta_{(-2\omega;\omega,\omega)}>(10^{-30})$ e.s.u	18.8866
Static Second order $<\Upsilon_{(0;0,0)}>(10^{-36})$ e.s.u	6.49490
Dynamic Second order $<\Upsilon_{(-\omega;\omega,0)}>(10^{-36})$ e.s.u	8.95460
Dynamic Second order $<\Upsilon_{(-2\omega;\omega,\omega)}>(10^{-36})$ e.s.u	134.814
Dipole moment μ (Debye)	10.9844

conjugated framework. The high degree of electronic charge delocalization and the low band gaps favors these physical properties. Vibrational modes of molecule of this kind is expected to be active in both IR and Raman spectra even though the strongest band in FT-IR spectrum appears as weak band in FT-Raman spectrum of organic molecules containing conjugated π electrons and characterized by large values of molecular first hyperpolarizabilities [19]. The stretching vibration bands of imidazole ring at 1577, 1523, 1410 and 1016 cm^{-1} in FT-IR and at 1485, 1436 and 1182 cm^{-1} in FT-Raman spectrum shows evidence for the intramolecular charge transfer.

4.7. Z-scan studies

The Z-scan is a highly sensitive technique employed for measuring the third order optical nonlinearity of materials. We measured the nonlinear absorption of L-HTFB in D_2O using open-aperture Z-scan. A Q-switched Nd:YAG laser emitting 5 ns, 532 nm pulses is used for exciting the sample. The linear transmittance of the sample is 80% at the excitation wavelength, when taken in a 1 mm cuvette. The laser beam is focused using a lens, and the sample transmission is measured at different positions (z) with respect to the beam focus (z=0). The normalized transmittance of the sample as a function of z is given by,

$$T(z) = \left(\left(1-R^2\right)\frac{e^{(-\alpha_0 L)}}{\sqrt{\pi q_0}}\right)\int_{-\infty}^{+\infty} ln[1+q_0 e^{(-t^2)}]dt \quad (1)$$

where L and R are the length and surface reflectivity of the sample, respectively. α is the linear absorption coefficient. $q_0 = \beta(1-R)\, I_0 L_{eff}$, where β is the effective two-photon absorption (2PA) coefficient, I_0 is the on-axis peak laser intensity and $L_{eff} = (1-e^{-\alpha L})/\alpha$.

The optical limiting curve extracted from the Z-scan data, showing the reduction of the normalized transmittance as a function of input laser fluence, is shown in Fig. 7a. The Z-scan curve is given as the inset, Fig. 7b. Solid curves show the best numerical fit to the measured data obtained using Eqn. (1). From the best fit, the effective two-

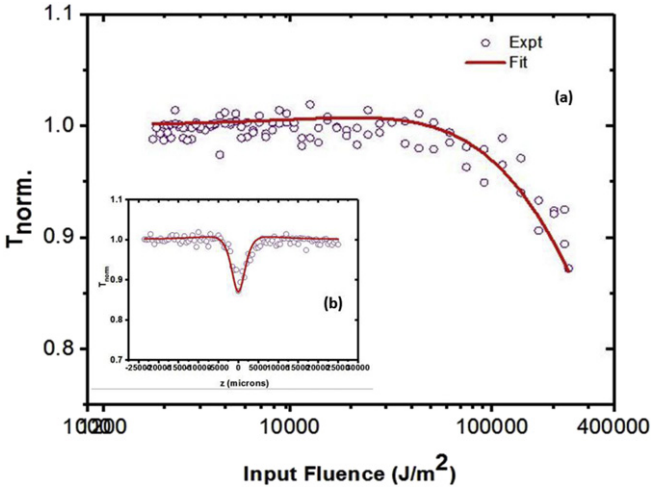


Fig. 7. (a) Open apertures Z-scan data (b) optical limiting property of L-HTFB.

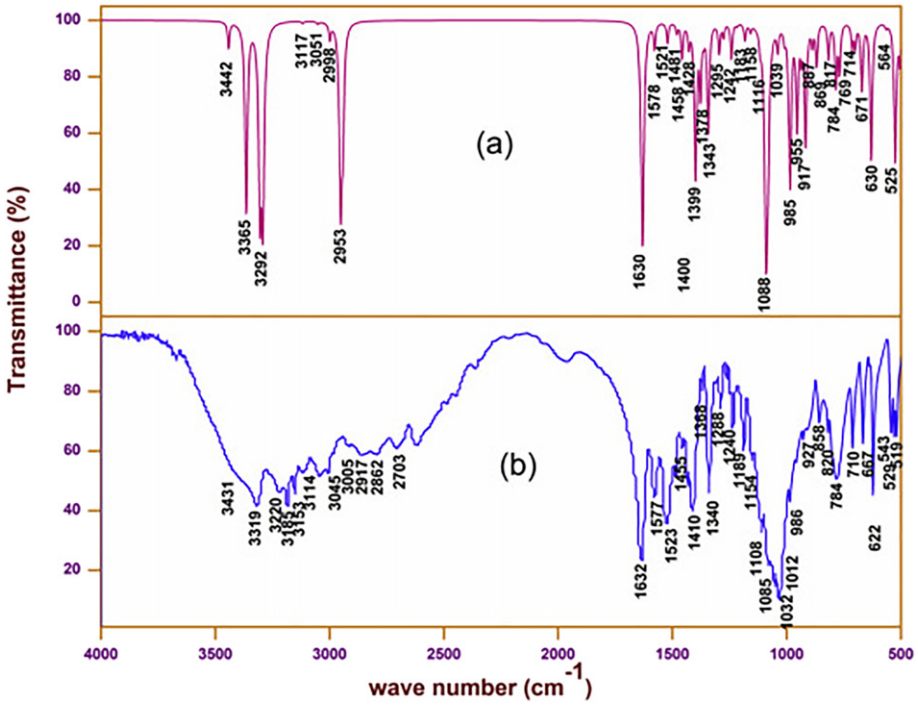


Fig. 8. FT-IR spectra (a) Theoretical (b) Experimental of L-HTFB.

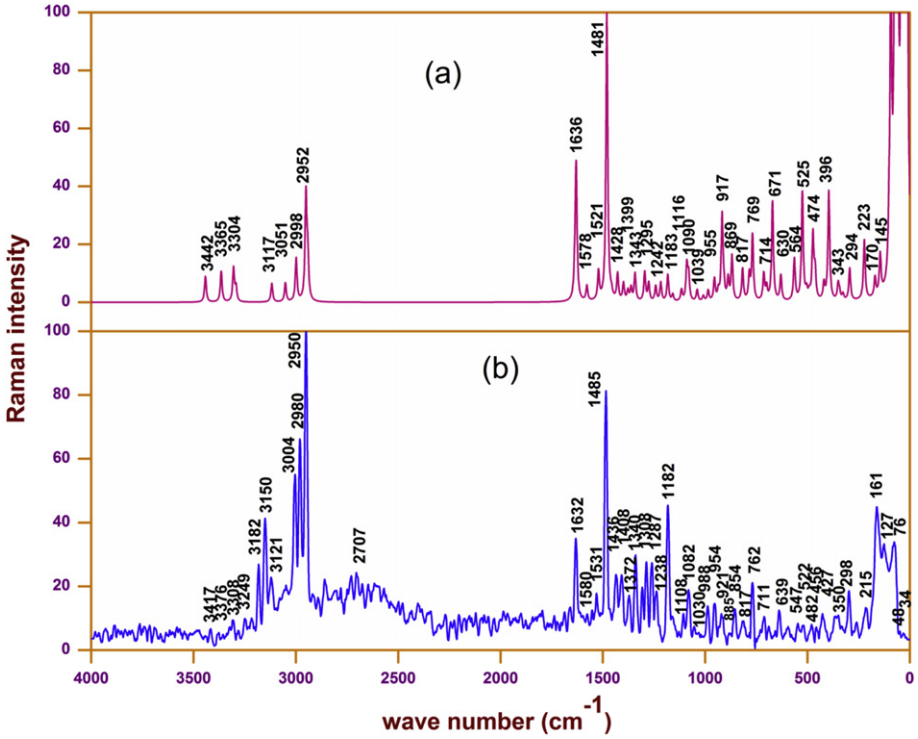


Fig. 9. FT-Raman spectra (a) Theoretical (b) Experimental of L-HTFB.

photon absorption coefficient (β) is found to be 1.0×10^{-10} m/W, which is a fairly high value when compared to benchmark optical limiters [18]. Therefore, the L-HTFB molecule turns out to be an efficient optical limiter. Optical limiters have extensive applications in pulse compression, passive mode-locking, and eye and optical sensor protection from high energy laser radiation. This high nonlinear absorption coefficient supports the strong π conjugation revealed from NBO analysis.

4.8. Interpretation of the spectra

The unambiguous assignment of vibrational modes are given on the basis of experimental IR and Raman spectra, simulated vibrational wavenumbers, normal coordinate analysis followed by Gaussian force field calculation and scaled quantum mechanical force field (SQMFF) methodology with Potential Energy Distribution data. The SQMFF procedure is essential to avoid the systematical error due to the

Table 5
Calculated vibrational wavenumbers, observed IR and Raman frequencies and their assignments with PED % for LHTFB.

Mode No.	Calculated (DFT)			Observed (cm^{-1})		Assignment (% PED, internal coordinates having contribution ≥10% are shown)
	ν_{Scal} (cm^{-1})	I_{IR} (%)	I_R (%)	FT-IR	FT-Raman	
1	3442	100.00	55.06	3431 w	3417 w	Imz[νNH(96)]
2	3365	14.28	61.10	-	3376 w	Imz[νNH(97)]
3	3304	58.55	63.33	3308 w	3324 w	νNH_{ss}(100)
4	3292	16.88	26.29	3217 w	3249w	νNH_{as}(99)
5	3117	18.55	29.19	3114 w	3121 m	Imz[νCH(93)]
6	3051	52.25	27.51	3045 w	-	νCH_{as}(93)+ νCH_{ss}(46)
7	2998	25.14	60.30	3005 w	3004 s	Imz[νCH(63)]
8	2952	32.90	44.76	-	-	Imz[νCH(59)]
9	2950	4.04	100.00	-	2980 s	Imz[νCH(68)]
10	2942	4.42	54.17	2917 w	2950 vs	Imz[νCH(99)]+ νCH_{ss}(84)+ νCH_{as}(46)
11	1636	2.12	8.68	1632 vs	-	δNH_{sci}(56)+ νCO_{as}(29)+ Imz[νCC(7)]+ δCO_{roc}(6)
12	1630	6.62	45.79	-	1632 s	νCO_{as}(50)+ δNH_{sci}(36)+ δCO_{roc}(3)
13	1578	3.54	4.92	1577 m	1580 w	Imz[δCH(60)]+Imz[νCC(59)]+Imz[νCN](27)+Imz[δCN](11)
14	1521	0.70	8.77	1523 s	1531 w	νFH (53)+ δNHF_{inter1} (13)
15	1481	0.76	85.15	1484 w	1485 vs	Imz[δCH (50)]+ νCO_{ss}(50)+ Imz[νCN](48)+ δCH_{sci}(34)
16	1458	1.79	1.56	1455 w	-	δCH_{sci}(28)+ Imz[δCN(12)]
17	1428	12.10	7.30	1433 w	1436 m	Imz[δCC(68)]+ Imz[δCN (43)]+ νCO_{ss}(35)+ Imz[νCN(14)]
18	1399	1.80	4.64	1410 s	1408 m	$\delta N^{+}H$ (34) +Imz[δCC](28)+ NH_{wag}(18)+ νOH_{str}(13)
19	1378	3.09	2.63	1368 w	1372 m	δCH_{asyd}(27) + NH_{wag}(10)+ δCO_{roc}(8)+ δNH_{roc}(7)+ νOH_{str}(7)
20	1362	7.23	3.30	1340 vs	-	δCH_{wag}(17)+ Imz[νCN(9)] + NH_{wag}(7)
21	1343	0.39	6.89	-	1340 s	Imz[δCH (24)]+ δCH_{twi}(15) +δCH_{wag}(9)
22	1295	0.43	6.85	1288 m	1308 m	Imz[δCH (37)]+ δNH_{wag}(24)+ Imz[νCC(7)]
23	1276	1.02	4.13	-	1287 m	δCOH(26) + Imz[νCC(15)] + νCO_{ss}(7)+ δCO_{syd}(5)
24	1242	12.03	3.31	1240 s	1238 w	δCH_{asyd}(29)+ δCH_{syd}(18)+ Imz[νCC(10)]+ δCOH(9)
25	1217	4.63	3.97	-	-	Imz[νCC(11)]+ δCH_{wag}(9)
26	1183	2.81	5.42	1189 m	1182 s	δCOH(36)+ Imz[νCN(17)]+ δCH_{syd}(14)+ Imz[δCH(6)]
27	1158	11.01	1.33	1154 w	-	Imz[δCH(37)] +νCN(32)+ δCH_{asyd}(7)+ Imz[δCN_{sydo}(7)] + δCOH(6) + δNH_{roc}(5)
28	1116	1.43	2.08	1108 w	-	δNH_{roc}(25)+ νCN(15)+ δCOH(11) + δCH_{syd}(10)
29	1090	2.93	6.19	-	-	δCH_{syd}(12)+ δFBF_{asyd}(10)+ δFBF_{roc}(9)
30	1083	7.23	1.28	1085 w	1082 m	νBF_{ip}(55)+ δCH_{syd}(35)+ νCN(15)+ δCH_{asyd}(8)
31	1080	2.80	3.42	-	-	δCH_{roc}(29)+ νCN(15)+ Imz[δCN(7)]+ δCOH(7)+ δCH_{asyd}(6)
32	1039	3.51	1.89	1032 vs	1030 vw	δCH_{roc}(39)+Imz[νCN(18)]+ νCC(18)+ Imz[δCH(13)]+ δCCN_{xczd}(7)
33	1009	4.95	0.85	1016 s	1012 w	Imz[νCN(27)]+ Imz[δCH(13)]
34	985	2.37	1.63	986 w	988 m	νBF_{op}(30)+ Imz[νCN(13)] + δFBF_{asydo}(7)+ Imz[δCN_{syd}(6)] +δFBF_{roco}(6)+ νCC(6)
35	955	1.22	3.18	958 w	954 m	νBF_{op}(33)+ Imz[νCN(11)] + δFBF_{asydo}(7)+ δFBF_{roco}(7)
36	936	9.42	1.27	927 w	-	δCH_{roc}(39)+ νCC(11)+ δCH_{twi}(10)+ δCOH(8)
37	917	1.00	11.68	-	921 w	δFBF_{syd}(41)+ νBF(32)+ Imz[gCH(16)]+ νBF_{ss}(17)+ νBF_{ip}(10)
38	909	2.43	1.49	-	-	νCN(20)+ CH_{wag}(16)+ Imz[τCN(9)]+ Imz[δCN_{sydo}(5)]
39	888	1.18	2.79	-	885 vw	Imz[δCN_{sydo}(20)]+ δCCN_{xczd}(8)+ Imz[νCN(7)] + Imz[δCN_{syd}(6)] + Imz[gCN(5)]+ NH_{wag}(5)
40	869	0.60	5.65	858 m	854 w	δCCN_{xczd}(15)+ νCN(15)+ νCC(9)+ CO_{wag}(7)+ δCCN_{yczd}(6)
41	817	1.27	3.67	820 w	817 w	δCH_{twi}(19)+ νCN(6)+ νCC(6)+ δCXY_{sci}(4)
42	784	2.16	2.76	784 s	-	Imz[gCH(26)] + δCO_{syd}(21)+ νCC(19)+ δCCN_{xczd}(7)+ CH_{wag}(6)
43	769	0.81	6.90	-	762 m	νCC(12)+δCO_{syd}(62)+ δCOH(18)
44	714	3.86	2.52	710 m	711 w	νBF_{ss}(66)+ νBF_{ip}(15)+ νBF(14)
45	700	1.25	1.19	-	-	δNHF_{inter1} (16)+ $\tau_{FHinter1}$ (8)+ CO_{wag}(7)+ δCH_{asyd}(7)+ δCH_{syd}(5)
46	671	0.75	8.62	667 s	-	NH_{wag}(30)+ δNHF_{inter1} (27)+ $\tau_{FHinter1}$ (10)+ Imz[gCN(10)]+ $\tau_{FHinter2}$ (9)
47	630	2.97	2.01	622 vs	639 w	νCC(14)+ Imz[τCN_{asy}(12)]+ Imz[δCN_{sydo}(6)]
48	564	2.08	2.83	543 s	547 w	δCOH(22) + δCO_{roc}(20)+ δCCN_{xczd}(17)+ νCC(16)+ δCO_{syd}(11)
49	525	1.67	6.61	529 s	522 m	NH_{wag}(25) + Imz[δCN_{syd}(16)] + νCC(18)+ δCCN_{xczd}(6)
50	505	2.00	0.53	519 s	516 w	τ_{NH3}(28) +δFBF_{roc}(21)+ δFBF_{asyd}(20)+ δFBH (9)+ δFBF_{syd}(8)+ νBF_{ip}(5)
51	493	3.24	0.22	-	-	δFBF_{asydo}(21)+ δFBF_{roco}(21)+ νBF_{op}(8)+ δFBF_{asyd}(8)+ δFBF_{roc}(7)+ δFBF_{syd}(6)
52	490	3.07	0.20	-	482 m	δFBF_{asyd}(46)+ νBF(12)+ νBF_{ss}(7)+δFBF_{asydo}(6) δFBF_{roco}(5)
53	474	1.43	3.42	-	477 w	δCCN_{xczd}(21)+ τ_{COOH} (18) + δCCN_{yczd}(10) + CO_{wag}(8) + νCC(6)
54	463	1.12	1.41	-	456 vw	δCO_{roc}(60)+ δCOH(15) + δCCN_{xczd}(8)
55	420	1.93	0.71	-	427 w	τ_{NH3}(46)+τ_{COOH} (21)+ δNHF_{inter2}(16) +νFH(6)
56	396	2.93	4.38	-	-	Imz[τCN_{sy}(27)]+ τ_{NH3}(20)+τ_{COOH} (18)+ Imz[τCN_{asy}(17)]+ δNHF_{inter1}(5)
57	350	0.60	0.54	-	350 w	Imz[gCC(26)]+ τ_{C4C7}(24)+ τ_{ImzE} (13)+ τ_{NH3}(10)
58	343	32.03	0.22	-	-	δFBF_{asyd}(36)+ δFBF_{roc}(30)+ δFBF_{roco}(7)+ δFBF_{asydo}(6)+ δNHF_{inter2}(6)
59	327	3.14	0.19	-	-	δCO_{roc}(18)+ Imz[τCN_{sy}(10)]+ νFH(8)
60	294	1.65	0.81	-	298 m	δCCN_{yczd}(32) + δCCN_{xczd}(29) + δCCN_{xcyd}(28) δFBF_{roco}(19)+ δFBF_{asydo}(15)+ δFBF_{roc}(6)+ δFBF_{asyd}(5)
61	223	14.49	0.97	-	215 w	δCCN_{yczd}(10) + δCCN_{xczd}(9) + δCCN_{xcyd}(8)+ τ_{NH3}(8) + τ_{COOH} (7)+ δCCN_{yczd}(7)
62	170	2.73	0.20	-	-	δCO_{roc}(37)+ νOH(29)+ τ_{COOH} (9)+ δCOH(5)
63	145	4.54	0.31	-	161 vs	νFH(37)+ νOH(31)+ δCO_{roc}(20)+ τ_{COOH} (8)+ δCOH(6)
64	101	8.33	0.15	-	127 w	νOH(39)+ δCO_{roc}(33)+ δCCN_{xcyd}(8)+ δCOH(5)
65	93	3.71	1.03	-	-	νOH(43)+ δCO_{roc}(32)+ δCCN_{xcyd}(8)+ δCOH(6)
66	76	4.78	0.55	-	76 s	νFH(27)+ τ_{COOH} (26)+ δCO_{roc}(17)+ τ_{C7C8}(12)+ νOH(7)+ τ_{ImzE} (5)
67	64	2.07	0.82	-	-	δCO_{roc}(21)+ τ_{COOH} (19)+ νOH(10)+ τ_{C7C8}(10)+ τ_{ImzE} (8)
68	58	2.07	0.25	-	-	νOH(26)+ τ $NHFB_{inter1}$ (10)+ δCO_{roc}(9)+ τ_{C4C7}(8)+ νFH(7)+ δCCN_{xczd}(7)
69	42	1.57	0.12	-	48 vw	τ_{BF4} (38)+ τ_{NH3}(10)+ νFH(8)+δFBH (9)
70	37	3.75	0.33	-	-	νOH(42)+ δCO_{roc}(23)+ τ_{NH3}(10)+ δCCN_{xczd}(6)
71	36	3.41	0.07	-	34 vw	νOH(36)+ δCO_{roc}(16)+ τ_{NH3}(12)+ τ_{NF} (8)
72	16	2.86	0.11	-	-	νOH(36)+ δCO_{roc}(17)+ τ_{NH3}(13)+ νFH(7)+ δFBH (7)+ δCCN_{xczd}(5)

Imz, Imidazole ring; ν, stretching; ss, symmetric stretching; as, asymmetric stretching; δ, bending; roc, rocking; roco, out of plane rocking; sci, scissoring; wag, wagging; puck, puckering; twi, twisting; syd, symmetric deformation; sydo, out of plane symmetric deformation; asyd, asymmetric deformation; asydo, out of plane asymmetric deformation; xcyd, deformation in xy direction; xczd, deformation in xz direction; yczd, deformation in yz direction; g, gauche out of plane deformation; τ, torsion; τ_o, out of plane torsion; inter1, N10-H16···F25; inter2, N11-H17···F22 .

Table 6
Bond critical point of LHTFB.

Type (BCP)	ρ (a.u.)	$\nabla^2\rho$ (a.u.)	V (a.u.)	G (a.u.)	H (a.u.)	$\|V\|/G$	K	λ1	λ2	λ3	$\|\lambda1\|/\lambda3$	ε
N10-C3	0.292	-0.788	-0.554	0.178	-0.376	3.104	0.376	-0.580	-0.523	0.315	1.842	0.109
C3-C2	0.342	-1.003	-0.522	0.136	-0.386	3.851	0.386	-0.762	-0.532	0.291	2.617	0.432
C3-C4	0.258	-0.638	-0.283	0.062	-0.221	4.576	0.221	-0.500	-0.482	0.345	1.452	0.038
H5-C4	0.277	-0.929	-0.313	0.040	-0.273	7.741	0.273	-0.725	-0.714	0.510	1.423	0.015
C4-H6	0.279	-0.952	-0.315	0.039	-0.277	8.181	0.277	-0.744	-0.739	0.531	1.402	0.006
C4-C7	0.243	-0.554	-0.251	0.056	-0.195	4.462	0.195	-0.462	-0.448	0.355	1.299	0.031
C7-C8	0.235	-0.513	-0.233	0.053	-0.181	4.443	0.181	-0.467	-0.434	0.388	1.203	0.075
C1-N9	0.281	-0.750	-0.527	0.170	-0.357	3.104	0.357	-0.580	-0.468	0.298	1.945	0.241
N9-C2	0.289	-0.771	-0.555	0.181	-0.374	3.064	0.374	-0.572	-0.515	0.316	1.808	0.110
N10-H14	0.019	0.061	-0.011	0.013	0.002	0.861	-0.002	-0.022	-0.018	0.101	0.215	0.180
C1-N10	0.285	-0.765	-0.539	0.174	-0.365	3.100	0.365	-0.594	-0.476	0.304	1.952	0.248
N11-C7	0.239	-0.571	-0.396	0.127	-0.269	3.124	0.269	-0.432	-0.410	0.271	1.591	0.053
C8-O13	0.396	-0.358	-1.228	0.569	-0.659	2.157	0.659	-1.016	-0.958	1.616	0.629	0.060
O12-C8	0.374	-0.433	-1.099	0.496	-0.604	2.218	0.604	-0.912	-0.887	1.366	0.668	0.029
H15-O12	0.051	0.146	-0.048	0.042	-0.006	1.136	0.006	-0.083	-0.078	0.307	0.270	0.060
H14-N11	0.328	-1.689	-0.511	0.044	-0.467	11.497	0.467	-1.256	-1.247	0.814	1.542	0.007
H15-N11	0.300	-1.534	-0.476	0.046	-0.430	10.327	0.430	-1.148	-1.146	0.760	1.511	0.002
H16-N10	0.331	-1.700	-0.521	0.048	-0.473	10.839	0.473	-1.285	-1.232	0.817	1.573	0.043
H17-N11	0.326	-1.753	-0.523	0.042	-0.481	12.328	0.481	-1.276	-1.268	0.792	1.612	0.006
C2-H18	0.284	-0.992	-0.320	0.036	-0.284	8.906	0.284	-0.781	-0.746	0.534	1.462	0.047
H19-C1	0.277	-0.930	-0.314	0.041	-0.273	7.719	0.273	-0.750	-0.696	0.515	1.455	0.078
H20-N9	0.339	-1.599	-0.512	0.050	-0.456	10.271	0.456	-1.272	-1.211	0.884	1.438	0.050
C7-H21	0.282	-0.964	-0.318	0.039	-0.280	8.249	0.280	-0.759	-0.731	0.526	1.442	0.038
F22-H17	0.030	0.114	-0.027	0.028	0.001	0.968	-0.001	-0.044	-0.043	0.201	0.221	0.031
B26-F25	0.152	0.740	-0.368	0.276	-0.091	1.330	0.091	-0.351	-0.344	1.435	0.244	0.018
B26-F22	0.147	0.707	-0.352	0.264	-0.087	1.331	0.087	-0.329	-0.324	1.359	0.242	0.015
F24-B26	0.158	0.774	-0.388	0.291	-0.097	1.334	0.097	-0.373	-0.368	1.515	0.246	0.013
F25-H5	0.006	0.022	-0.004	0.005	0.001	0.823	-0.001	-0.005	-0.004	0.031	0.163	0.199
F25-H16	0.020	0.079	-0.016	0.018	0.002	0.901	-0.002	-0.026	-0.025	0.131	0.201	0.040
F23-B26	0.171	0.872	-0.436	0.327	-0.109	1.334	0.109	-0.438	-0.435	1.745	0.251	0.006

Table 7
Ring critical point of LHTFB.

SL.No	Type (RCP)	ρ (a.u.)	$\nabla^2\rho$ (a.u.)	V (a.u.)	G (a.u.)	H (a.u.)	$\|V\|/G$	K	λ1	λ2	λ3
I	C3-C4-C7-N11-H14-N10	0.013	0.065	-0.010	0.013	0.003	0.771	-0.003	-0.011	0.016	0.060
II	C1-N9-C2-C3-N10	0.049	0.359	-0.073	0.081	0.008	0.898	-0.008	-0.053	0.185	0.228
III	C3-C4-H5-F25-H16-N10	0.005	0.022	-0.003	0.004	0.001	0.753	-0.001	-0.003	0.007	0.019
IV	C7-C8-O12-H15-N11	0.033	0.212	-0.039	0.046	0.007	0.848	-0.007	-0.038	0.084	0.166
V	N10-H14-N11-H17-F22-B26-F25-H16	0.004	0.019	-0.003	0.004	0.001	0.757	-0.001	-0.002	0.003	0.018

mechanical anharmonicity. The selective scaling procedure is performed after the normal coordinate analysis (NCA) to compensate the short comings and to match the calculated vibrational frequencies with the experimental data. The NCA is executed to reduce its RMS error up to 7 and to interpret the molecular motion using the MOLVIB program version 7.0. The observed FT-IR, FT-Raman along with the simulated vibrational spectra of L-HTFB is shown in Figs. 8 and 9. The total internal coordinates of L-HTFB are charted on Table S2. The force constants and the scale factors obtained after defining the local symmetry coordinates in the DFT/CAM-B3LYP/6–311++g(d,p) level of theory is summarized in the Table S3. The predicted wave numbers of fundamental modes of vibrations along with PED description is enclosed in Table 5. Assignments are given on the basis of vibrations due to L-histidinium ($C_6H_{10}N_3O_2^+$) and tetra fluro borate $(BF_4)^-$ complexes. The internal vibrational bands can be assigned on the basis of characteristic vibrations of ethyl, $C_3N_2H_4^+$, NH_3^+, COO^- and BF_4^- groups. The vibrational analyses of different functional groups are discussed below.

4.8.1. Ethyl vibration

Ethyl molecule is attached to $C_3N_2H_4^+$, NH_3^+, COO^- groups. The most intense Raman band observed at 2950 cm^{-1} is assigned to the stretching modes of CH_2 group. The vibrational bands due to CH of ethyl and imidazole are close to the ones of CH_2. The frequencies due to νCH_2, δCH_2, τ CH_2, CH_{wag}, are also assigned in comparison with optimized geometry (Table 3). The vibration of CH asymmetric bending mode is observed in Raman spectra at 1372, 1238 cm^{-1} and in IR spectra at 1368, 1240 cm^{-1}. The CH symmetric bending vibration is observed at 1085 and 1082 cm^{-1} in both IR and Raman spectra. The CH twisting vibration is observed at 1340 cm^{-1} in IR and Raman spectra. The CH rocking vibration mode observed as medium intense band at 1032 cm^{-1} and 927 cm^{-1} in IR spectra. The strong IR band at 622 cm^{-1} and Raman band at 639 and 762 cm^{-1} are assigned to the ethyl C-C stretching and is red shifted from the imidazole ring C-C stretching modes due to the linkage of different stretching and bending interactions [20]. The ethyl chain deformation vibration in the direction XY, XZ and YZ are observed as weak intense band at 215 and 298 cm^{-1} respectively. The band at 1455 cm^{-1} assigned to the CH scissoring vibration mode.

4.8.2. Imidazole ring vibrations

4.8.2.1. C-H vibrations. The vibrational bands due to CH of ethyl and imidazole are close to the ones of CH_2. The C-H stretching vibrations of the imidazole ring are distinctly observed as strong band in Raman at 2950 cm^{-1} and as weak band in IR at 2917cm^{-1} as expected. The

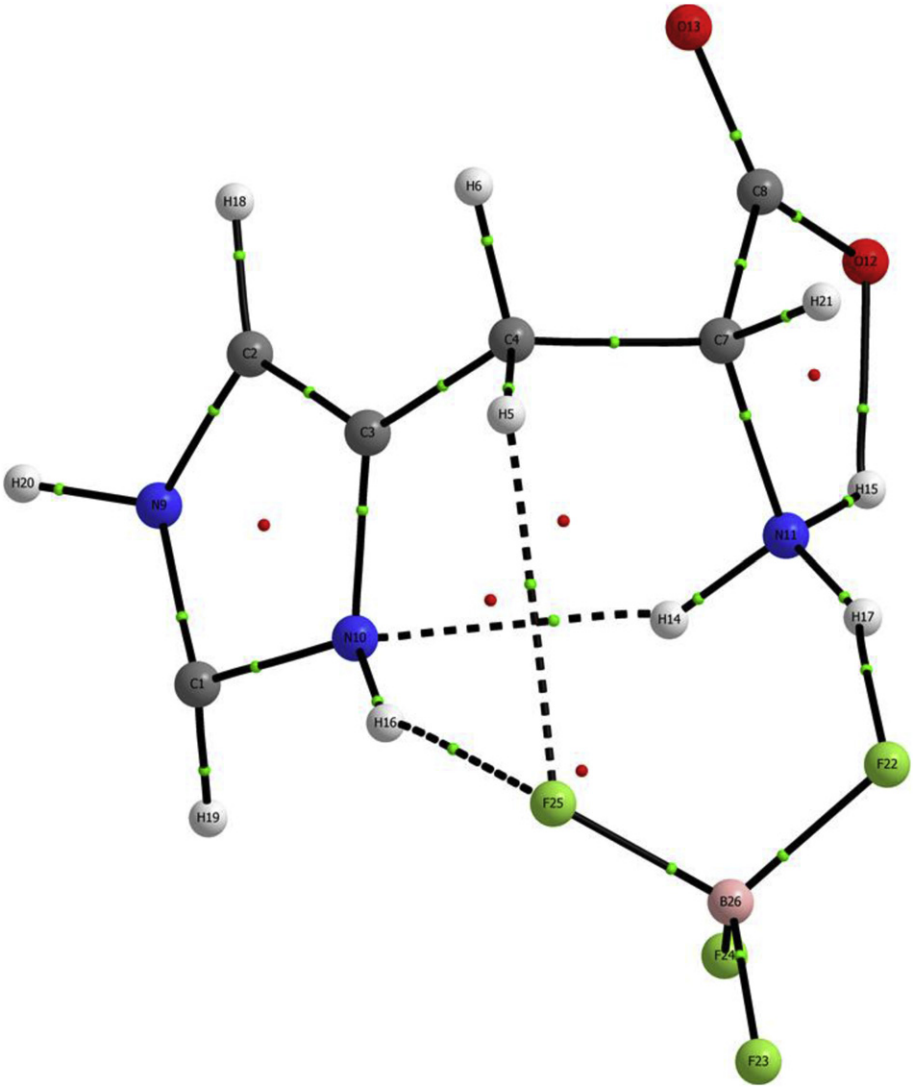


Fig. 10. Molecular structure with bonded atoms by the electron density concentration at equilibrium geometry of L-HTFB.

imidazole C-H in plane bending vibration modes occur at 1577, 1340, 1288 cm^{-1} in IR and 1308, 1485, 1154, 1016 cm^{-1} in Raman spectrum are coupled with other modes. The out of plane wagging vibration is observed as weak band at 921 cm^{-1} in Raman and as strong band at 784 cm^{-1} in IR spectra as expected [21].

4.8.2.2. N-H vibrations. The $\delta N^{+}H$ expected around 1415 cm^{-1} is observed as a strong band at 1410 cm^{-1} in IR and as a medium intense band at 1408 cm^{-1} in Raman. The shoulder at 2703 is assigned to $\nu N^{+}H$. The observation of $\delta N^{+}H$ and $\nu N^{+}H$ indicates the protonation of nitrogen atom.

4.8.2.3. C-C vibrations. Generally C-C and C-N stretching vibrations of imidazoles have three or four bands in the region 1670-1320 cm^{-1} The C-C stretching vibration appears as medium intense IR band at 1577 cm^{-1} and weak Raman band at 1580 cm^{-1}. The corresponding value is estimated to be to 1578 cm^{-1} in the DFT calculation. This band is complement in both the theoretical as well as experimental spectrum. Also, the in-plane deformation vibration of C-C bond mixed with its stretching vibrational mode are observed at 1436, 1408 cm^{-1} in Raman and 1433, 1410 cm^{-1} in IR spectrum. In comparison, the in plane bend vibrations are at higher wave number than the out of plane vibration at 350 cm^{-1} in Raman.

4.8.2.4. C-N vibrations. The two C-N stretching vibrational modes in imidazole ring is observed at 1577 and 1484 cm^{-1} IR and 1580 and 1485 cm^{-1} in Raman spectra. The protonated CN in plane bending vibration appears as weak IR band at 1433 cm^{-1} and medium intense Raman band at 1436 cm^{-1}. These vibrational modes depend on the heterocyclic resonance effect which results in the delocalization of π → π*electrons as mentioned in NBO analysis.

4.8.3. Amino group vibration

A broad asymmetric band is observed in the 3400–2550 cm^{-1} with maximum at 3153 cm^{-1} and several shoulders on the low frequency side. Hence, this band has contributions from ν_s, $\nu_{as,}$ modes of NH_3^+ and ν_s, $\nu_{as,}$ modes of CH_2 group. The C-N stretching vibration occurs at 1154, 1016 in IR and 1082 cm^{-1} in Raman spectra.

The intra molecular hydrogen bonded interaction which happens due to the protonation effect of donor NH_3^+ and acceptor COO^- has vibrational modes as observed in amide frequency range. The N-H stretching vibrations occur in the region 3100-3500 cm^{-1} [22]. The N-

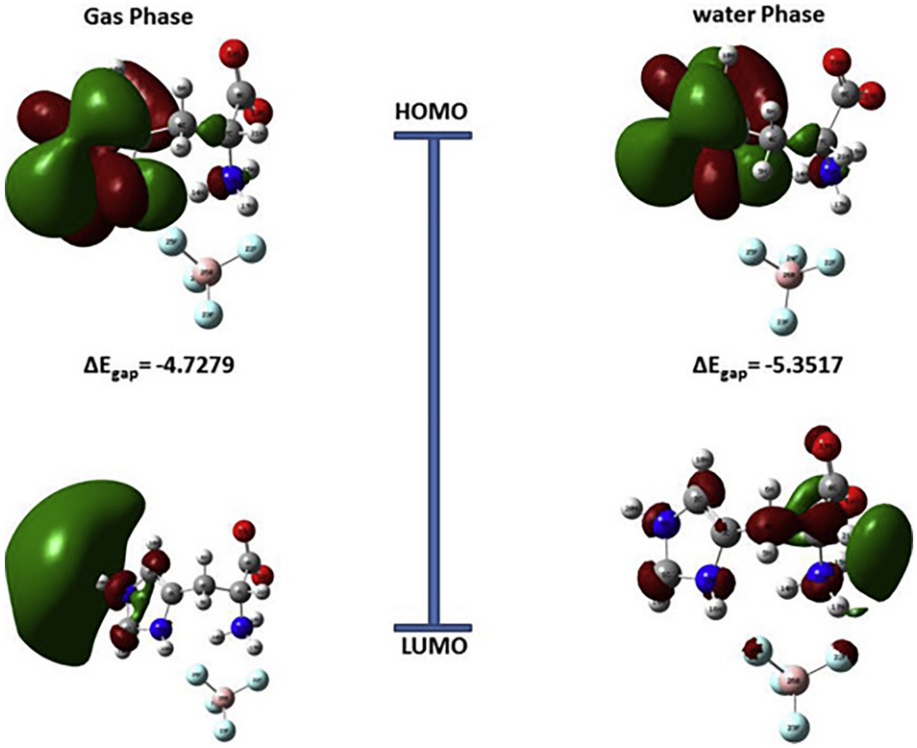


Fig. 11. Pictorial representation of the frontier molecular orbitals of L-HTFB in gas and water phase.

H asymmetric stretching in the NH_2 group band is observed in the FT-IR and FT-Raman at 3308 and 3324 cm^{-1} with 98% PED. The symmetric stretching appeared as weak intense band at 3249 cm^{-1} in FT-Raman and weak band at 3217 cm^{-1} in FT-IR spectra. The mode N-H scissoring occurs as strong band in the wavenumber 1632 cm^{-1} in FT-IR and FT-Raman spectra. The feeble band originate at 1108, 1085 cm^{-1} in FTIR and medium band at 1082 cm^{-1} in FT-Raman indicates the NH rocking mode mixed with other deformation vibrations. The NH wagging mode is observed as weak band at 1410, 1368, 1288, 667, 529 cm^{-1} in FT-IR spectrum. Also the torsion mode involving NH_3^+ is evident at 516, 215 cm^{-1}as weak intense FT-Raman band.

4.8.4. Carboxylate group vibrations

It is well known that the deprotonated carboxyl (COO^-) has two very characteristic absorption bands around 1600 and 1420 cm^{-1} due to the asymmetric and symmetric stretching modes respectively. In a non-dissociated carboxylic acid (COOH), the C=O and C-O stretching frequencies are expected around 1730 and 1250 cm^{-1} respectively [23]. The observation of very intense IR and Raman bands at 1632 cm^{-1} and 1485 cm^{-1} due to ν_{as} COO^- and ν_s COO^- respectively suggest the deprotonation of carboxylic acid group. The NH_2 group simultaneously becomes NH_3^+. This is further supported by all the investigation on this compound.

4.8.5. BF_4 vibration modes

The in plane ν_{as} BF_4 is observed as shoulder band at 1085 cm^{-1} in IR and medium intense band at 1082 cm^{-1} in Raman spectra. The IR band at 710 cm^{-1} and Raman band at 711 cm^{-1} are assigned to ν_s mode. The out of plane ν_{as} band occurs at 986 cm^{-1} in IR and 988 cm^{-1} in Raman spectrum. The symmetric deformation vibrational mode of BF_4 appeared at 921 cm^{-1} and the in plane asymmetric bending vibration appeared as medium band at 482 cm^{-1} and out-of-plane asymmetric deformation and rocking vibrations is observed as medium intense band at 298 cm^{-1} in Raman spectrum [24]. The torsion BF_4 vibration mode occurs at 48 cm^{-1} in Raman spectrum.

4.9. Intra and inter molecular interaction related vibration

The molecular interaction between the two present complexes L-H and BF_4 connected with the three F-H bond within the Vander Waal radii seemed as strongest intense band at 1523 cm^{-1} in IR spectrum of $F_{25}\cdots H_{16}$ stretching vibration mode and strong intense band at 161, 76 cm^{-1} in Raman spectrum of corresponding $F_{22}\cdots H_{17}$ and $F_{24}\cdots H_{14}$ stretching vibration modes. The intra-molecular interaction of $O_{12}\cdots H_{15}$ has OH stretching vibration mode and appears as strong band at 1410 cm^{-1} in IR and medium band at 1408 cm^{-1} in Raman spectra. The linkage of N-H...O along with a CO···H bending in intra molecular interaction is observed as medium band at 1287, cm^{-1} in Raman vibrational spectra.

4.10. AIM analysis

This is a tool used for investigating the nature of atoms in molecule (AIM) [25] with bonding interactions by the characteristics of the electron density critical point descriptors of the molecular structure,

Table 8
Calculated quantum chemical descriptors of LHTFB molecule using basis set CAM-B3LYP/6–311++g(d,p).

Parameters of LHTFB	Gas phase	Water phase
E_{HOMO} energy (eV)	-2.1863	-4.8739
E_{LUMO} energy (eV)	2.5416	0.4778
$\Delta E_{GAP}=E_{LUMO}$- E_{HOMO} (eV)	-4.7279	-5.3517
Ionisation potential, IA (eV)	2.1863	4.8739
Electron affinity, EA (eV)	-2.5416	-0.4778
Electronegativity, χ (eV)	-0.1776	2.1981
Chemical hardness, η (eV)	2.3640	2.6759
Global softness, S $(eV)^-$	0.2115	0.1869
Chemical potential, μ (eV)	0.1776	-2.1981
Electrophilicity index, ψ (eV)	0.0067	0.9028
Total energy change, ΔE_T (eV)	0.5910	0.6690
Overall energy balance, ΔE (eV)	-4.7279	-5.3517

specifically, the electron density (ρ), Laplacian of the electron density ($\nabla^2\rho$), gradient kinetic energy density (G), potential energy density (V), total energy density (H) and ellipticity(ε). Hence, the total number of electron density critical points is found as 61 and are divided into four 26 number of (3,-3) type nuclear attractor critical point (NACP), 30 number of (3,-1) type bond critical point (BCP), 5 number of (3,+1) type ring critical point (RCP) and the cage critical point (CCP) and Non-nuclear attractor critical point (NNACP) is set as zero numbers due to the absence in the molecular system. The electron density distributions among the critical points and the eigen values of the Hessian density matrix at BCP and RCP are enclosed in Tables 6 and 7. The molecular structure with bonded atoms through a path in which the electron density is concentrated maximum at equilibrium geometry is illustrated in Fig. 10. Obviously, the green beads indicate the bond critical points and the red beads indicate the ring critical points in the molecular structure sketch. The curvatures $\lambda_1$and $\lambda_2$become negative given that $|\lambda_1|>|\lambda_2|$ in which the charge density concentrated at BCP along the bond path while λ_3 is positive which denoting the depletion of the charge density and region of contact of the atomic basins. However, at RCP, the eigen values of the Hessian density matrix shows the curvatures $\lambda_3>\lambda_2$ and $-\lambda_1$are in Table 7. The strength of the bond is reflected through the magnitude of electron density function at BCP as greater value of electron density. In L-HTFB the electron density is maximum for the small $|V|/G$ ratios below '1' are in the order F_{25}-H_5 < N_{10}-H_{14}< F_{25}-H_{16} < F_{22}-H_{17} at BCP and in the order III < V < I < IV < II at RCP, reveals the depleted charge densities with the dominant kinetic energy densities. These kinds of changes in parameters are generally related with the closed-shell interactions. The Laplacian of the electron densities are positive for all RCP's (Table 7) reveals the localized concentration of electrons or the tendency of concentration of charge densities to a large extent at these points. The total energy density (H) consuming negative values indicate the stabilizing and attractive type of interaction in relation with the property of the very polarized bond. The electron density is maximum on N_{11}-H_{17} > N_{11}-H_{14} > N_{10}-H_{16} > N_{11}-H_{15} > N_9-H_{20} and the corresponding large negative value of $\nabla^2\rho$ showing its covalent nature. The BCP table and figure shows that the positive $\nabla^2\rho$ value of F_{23}-B_{26} > F_{24}-B_{26} > F_{25}-B_{26} > F_{22}-B_{26} in BF_4 group indicates that the three inter-molecular interaction affects as depletion in the $\nabla^2\rho$ electron density value than the normal F_{23}-B_{26} electron density. The highest ellipticity on the carbon skeleton C_2-C_3 in the imidazole ring reveals the extension of π-electron delocalization. The bond ellipticity indicates the measure of π-character bond and is second highest in the bond C_1-N_{10}.

4.11. HOMO-LUMO analysis

The electron absorption wave function incorporate with the transition of electrons from the orbitals in the ground state to the first excited state by one-electron excitation determine the molecular interaction and are the frontier molecular orbitals called highest occupied molecular orbital (HOMO) to the lowest unoccupied molecular orbital (LUMO). The electronic structure of L-HTFB is optimized in singlet state. The electronic based indices such as the global reactivity descriptors can be used to identify the response of the properties of the molecular system. The pictorial portrayal of the frontier molecular orbitals of L-HTFB in gas and water phase is in Fig. 11. The description of HOMO and LUMO analysis of the frontier molecular orbital and the global reactivity descriptors of L-HTFB in gas as well as water phase are set in Table 8. In both gas and water phase of the region spread over HOMO explains the charge distribution which is fully concentrated on the whole imidazole ring due to the delocalization of electrons. The transfer of charge from HOMO to LUMO is mostly concentrated on N-H bond in the imidazole ring in gas phase. Also, the distribution of charge from HOMO to LUMO is mostly concentrated on the COO, CH_2, NH_3 group, and slightly

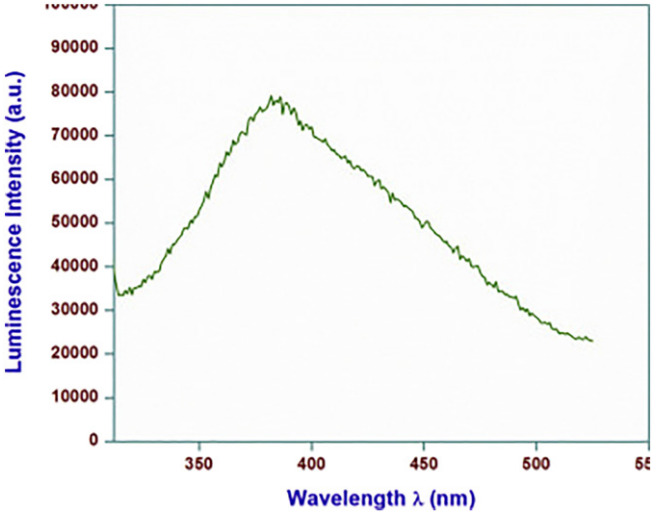


Fig. 12. Photoluminescence (PL) of LHTFB

concentrated on the two fluorine atoms of the BF_4 group as well as the atoms of the imidazole ring in water phase. The HOMO-LUMO energy gap -4.7279 eV and -5.3517 eV in gas phase as well as water phase discloses the effect of higher stabilization of LUMO as well as destabilization of HOMO indicates an enhanced intramolecular charge transfer interactions and thereby increases NLO activity in the system. The electronic transition states of π → π* type contributions has occurred in the HOMO to LUMO transitions [26]. The charge transfer and the extended π –conjugations leads to the low energy gap that influences the nonlinear optical processes of L-HTFB.

4.12. Photoluminescence

For organic compounds, the photoluminescence got wide usage in the branches of medical chemical and biochemical research fields [27]. The photoluminescence spectrum was recorded using PerkinElmer LS 55 Luminescence Spectrophotometer. The xenon lamp with high pressure operated at 450 W produces continuous output from 250nm to 600nm. The emission spectrum of excitation wavelength 275nm is shown in Fig. 12. The high intensity broad peak at 382 nm is originate from the π- π* transition of carbonyl group [28]. Generally, photoluminescence found in compounds including aromatic functional

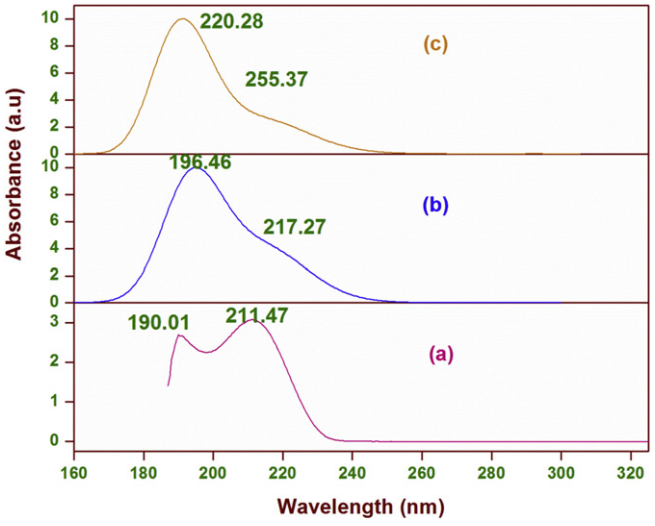


Fig. 13. UV–Vis spectra of L-HTFB (a) Experimental spectrum (b) Theoretical spectrum in gas phase and (c) Theoretical spectrum in water phase.

Table 9
Calculated absorption wave lengths, electronic excitation energies and oscillator strengths of L-HTFB.

Phase	Excited State	Wave length (nm)	Excitation energies (eV)	Oscillator Strength (f)
Gas phase	S1 (H→L)	255.37	4.8552	0.0112
	S2 (H→L+3)	225.19	5.5057	0.0133
	S3 (H→L+1)	220.28	5.6284	0.0387
	S4 (H-1→L)	208.91	5.9347	0.0103
	S5 (H→L+2)	202.50	6.1228	0.0001
	S6 (H-2→L)	197.68	6.2720	0.1047
Water Phase	S1 (H→L+1)	221.29	5.6027	0.0020
	S2 (H→L)	217.27	5.7066	0.0650
	S3 (H-1→L)	196.46	6.3109	0.1187
	S4 (H→L+2)	192.06	6.4554	0.0697
	S5 (H-1→L+1)	187.40	6.6160	0.0097
	S6 (H-2→L+1)	179.05	6.9246	0.0034

groups in the form of low energy π - π* transition levels [27]. The effect of photoluminescence clearly indicates that the L-HTFB crystal has a violet emission, so that it can be used as a new violet-light emitting material.

4.13. UV–Vis spectral analysis

The theoretical UV spectra in the gas phase and water phase along with experimental spectra in water phase of the L-HTFB molecule is enclosed in Fig. 13. The visible absorption wavelength maxima (λ) as a function of electron availability, excitation energies, and oscillator strengths has been reported in Table 9. The simulated electronic absorption spectra of the title molecule in gas phase shows two peaks at 220.28 nm (HOMO→LUMO+1) and 255.37 nm (HOMO→LUMO) with oscillator strength 0.0387 and 0.0112 a.u. The experimental electronic absorption spectrum of L-HTFB in water solvent shows two bands at 190.01 and 211.47 nm. The calculated electronic transitions in water phase points out the peak at 196.46 nm for HOMO – 1 → LUMO transition and 217.27 nm for HOMO → LUMO transition with oscillator strength 0.1187 and 0.0650 a.u. This shows that the computational spectra in gas phase as well as in water phase are in good agreement with the experimentally measured data. The effect of the substituent and the effect of the solvent shows slight shift in values from its experimental one. From this, the water phase absorption spectra influence more close to the experimental spectrum than the gas phase absorption spectra.

5. Conclusion

In this work, we have investigated the spectroscopic properties of the semi-organic stable complex L-histidine tetra fluroborate (L-HTFB). Experimental data and simulated IR and Raman spectra of L-HTFB are found to be in good mutual agreement with each other. From UV analysis, the substituents and the solvent effect are found to influence the water phase absorption spectra more closer to the experimental spectra, compared to the gas phase absorption spectra. Photoluminescence studies reveal that L-HTFB can be used as a new violet-light emitting material. The optimized crystal structure shows protonated five membered imidazole ring $(C_3N_2H_4)^+$ and $(NH_3)^+$ ions counterbalanced with negatively charged carboxylate $(COO)^-$ and tetrafluroborate $(BF_4)^-$ ions. Characteristic vibrations of these ions are found to be present in the IR and Raman spectra. Hirshfeld surface analysis of H ….F interactions of the compound exhibits 43.6% contribution. The difference in the lengths of the CO bonds reveals that there is N-H···O intra molecular interaction between one of the C-O bonds of COO^- and NH_3^+. AIM analysis reveals that the highest ellipticity on the carbon skeleton C_2-C_3 in the imidazole ring is due to the extension of π-electron delocalization. NBO analysis gives evidence for the existence of $C_2{=}C_3$ double bond as well as protonated N atom in the imidazole ring. The charge transfers as well as the extended π – conjugations cause the low energy gap which enhances the nonlinear optical property of L-HTFB. The enhancement of all the calculated static and dynamic hyperpolarizabilities compared to that of urea indicates that L-HTFB is a highly nonlinear material. The large value of γ hyperpolarizability, the intramolecular charge transfer (resulting from the electron cloud movement through donor-acceptor π conjugated framework) and the low band gaps enhance the non-linear optical properties of the crystal. The high nonlinear absorption coefficient measured for L-HTFB from open aperture Z-scan is in agreement with the strong π conjugation obtained from NBO analysis, and indicates its potential application in efficient optical limiting. From the above results it can be concluded that L-histidine tetra fluroborate is a stable complex which can be used as a new violet-light emitting material, and that it shows a high nonlinear optical property, with potential application as an efficient optical limiter.

Acknowledgments

D.Sajan and R.Chitra (DS& RC) thanks the UGC-DAE Consortium for Scientific Research, Mumbai Centre,R-5 Shed, Bhabha Atomic Research Centre, Trombay, Mumbai 400085 INDIA for the financial support (UDCSR/ MUM/CD/CRS-M-238/2017/1007dt.16.01.2017). The author (DS) also acknowledge the DST-FIST program (SR/FST/College- 182/ 2013, November 2013 & FIST No.393 dated 25- 09–2014) to the Bishop Moore College Mavelikara for providing the UV–visible and Computational facilities. The author (DS) is highly grateful to Prof. T. Sundius for the Molvib program.

Appendix A. Supplementary data

Supplementary data to this article can be found online at https://doi.org/10.1016/j.saa.2019.117615.

References

[1] Z. Yuan, C.D. Entwistle, J.C. Collings, D. Albesa-Jové, A.S. Batsanov, J.A.K. Howard, N.J. Taylor, H.M. Kaiser, D.E. Kaufmann, S.Y. Poon, W.Y. Wong, C. Jardin, S. Fathallah, A. Boucekkine, J.F. Halet, T.B. Marder, Chem. Eur J. 12 (2006) 2758–2771.
[2] H.O. Marcy, M.J. Rosker, L.F. Warren, P.H. Cunningham, C. a Thomas, L. a Deloach, S.P. Velsko, C. a Ebbers, J.H. Liao, M.G. Kanatzidis, Opt. Lett. 20 (1995) 252–254.
[3] S. Gokul Raj, G. Ramesh Kumar, T. Raghavalu, R. Mohan, R. Jayavel, Acta Crystallogr. Sect. E Struct. Reports Online 62 (2006) 1178–1180.
[4] M. Sheik-Bahae, A.A. Said, T.H. Wei, D.J. Hagan, E.W. Van Stryland, IEEE J. Quantum Electron. 26 (1990) 760–769.
[5] P.R. Lee C, W. Yang, Phys. Rev. B 37 (1988) 785–789.
[6] D.E. Woon, T.H. Dunning, J. Chem. Phys. 98 (1993) 1358–1371.
[7] H.S.M. Frisch, G. Trucks, Gaussian, Inc. Wallingford, 2009.
[8] T. Sundius, Vib. Spectrosc. 29 (2002) 89–95.
[9] F.W.E. Glendening, J. Badenhoop, A. Reed, J. Carpenter, J. Bohmann, C. Morales, Theor. Chem. Insti, University of Wisconsin, Madison, 2001.
[10] S.G. Raj, G.R. Kumar, R. Mohan, S. Pandi, R. Jayavel, Mater. Chem. Phys. 90 (2005) 144–147.

[11] S.S. Batsanov, Inorg. Mater. 37 (2001) 871–885.
[12] P. Auffinger, F.A. Hays, E. Westhof, P.S. Ho, Proc. Natl. Acad. Sci. U.S.A. 101 (2004) 16789–16794.
[13] L. Pauling, The Nature of the Chemical Bond and the Structure of Molecules and Crystals : an Introduction to Modern Structural Chemistry, Cornell University Press, Ithaca, New York, 1960.
[14] A.E. Reed, L.A. Curtiss, F. Weinhold, Chem. Rev. 88 (1988) 899–926.
[15] Z.-X. Wang, C. Wu, H. Lei, Y. Duan, J. Chem. Theory Comput. 3 (2007) 1527–1537.
[16] J. Karpagam, N. Sundaraganesan, S. Sebastian, S. Manoharan, M. Kurt, J. Raman Spectrosc. 41 (2010) 53–62.
[17] T. Vijayakumar, I.H. Joe, C.P.R. Nair, V.S. Jayakumar, Chem. Phys. 343 (2008) 83–99.
[18] V. Sasikala, D. Sajan, L. Joseph, J. Balaji, S. Prabu, P. Srinivasan, Chem. Phys. Lett. 674 (2017) 11–27.
[19] C. Ravikumar, I.H. Joe, V.S. Jayakumar, Chem. Phys. Lett. 460 (2008) 552–558.
[20] M. Majoube, M. Henry, L. Chinsky, P.Y. Turpin, Chem. Phys. 169 (1993) 231–241.
[21] L. Colombo, P. Bleckmann, B. Schrader, R. Schneider, T. Plesser, J. Chem. Phys. 61 (1974) 3270–3278.
[22] G. Sokrates, Infrared and Raman Characteristic Group Frequencies : Tables and Charts, 2001.
[23] B.L. George, Sunila Abraham, G. Aruldhas, Indian J. Pure Appl. Phys. 32 (1994) 876–881.
[24] N.E. Heimer, R.E. Del Sesto, Z. Meng, J.S. Wilkes, W.R. Carper, J. Mol. Liq. 124 (2006) 84–95.
[25] R.F.W. Bader, Atoms in Molecules-A Quantum Theory, Oxford University Press, Oxford, 1990.
[26] P. Thanikaivelan, V. Subramanian, J.R. Rao, B.U. Nair, Chem. Phys. Lett. 323 (2000) 59–70.
[27] H.H. Willard, L.L.J. Merritt, J.A. Dean, F.A.J. Settle, Instrumental Methods of Analysis, seventh ed. Wadsworth Publishing company, Florence, KY (USA), 1988.
[28] G. Accorsi, A. Listorti, K. Yoosaf, N. Armaroli, Chem. Soc. Rev. 38 (2009) 1690–1700.